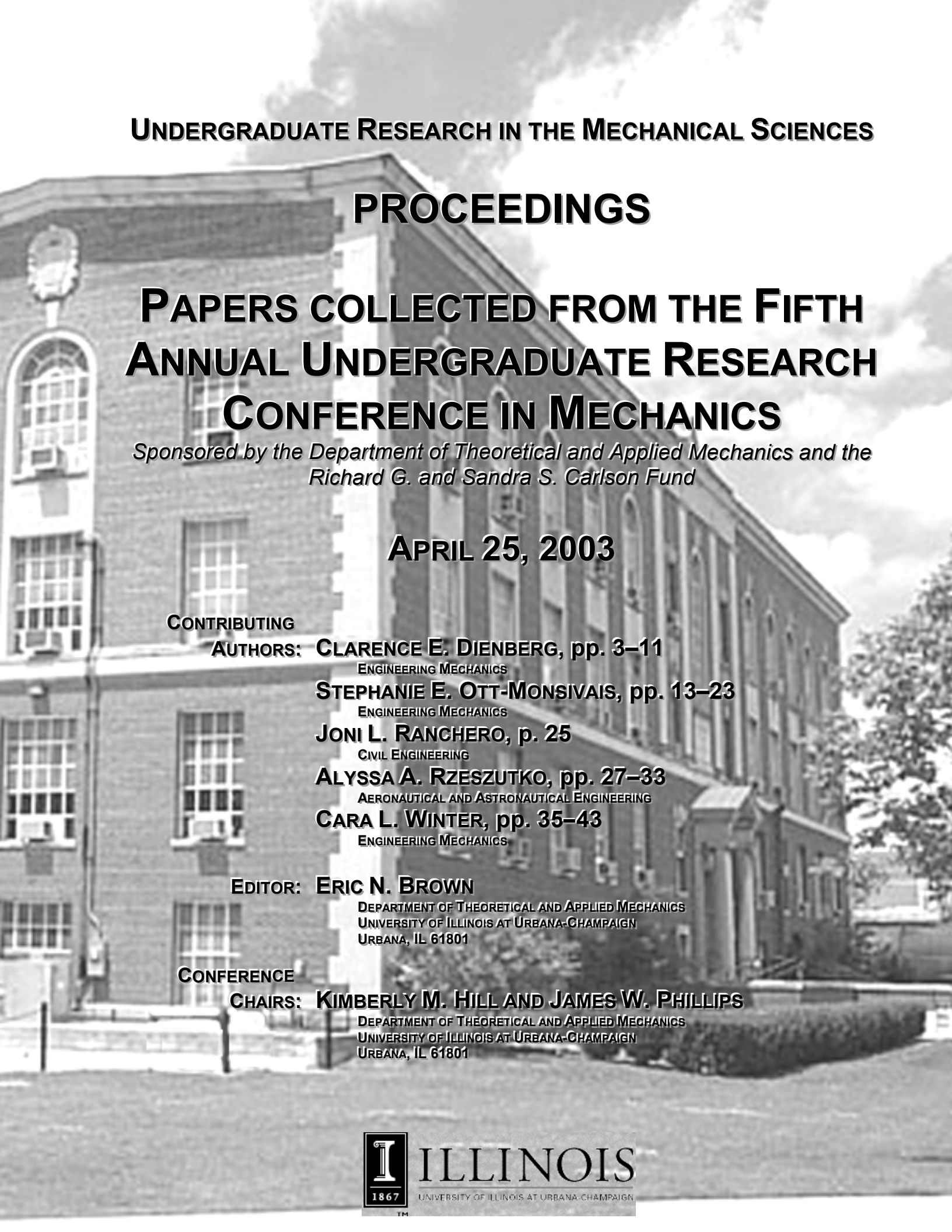

UNDERGRADUATE RESEARCH IN THE MECHANICAL SCIENCES

PROCEEDINGS

PAPERS COLLECTED FROM THE FIFTH ANNUAL UNDERGRADUATE RESEARCH CONFERENCE IN MECHANICS

Sponsored by the Department of Theoretical and Applied Mechanics and the Richard G. and Sandra S. Carlson Fund

APRIL 25, 2003

CONTRIBUTING AUTHORS:

CLARENCE E. DIENBERG, pp. 3–11
ENGINEERING MECHANICS

STEPHANIE E. OTT-MONSIVAIS, pp. 13–23
ENGINEERING MECHANICS

JONI L. RANCHERO, p. 25
CIVIL ENGINEERING

ALYSSA A. RZESZUTKO, pp. 27–33
AERONAUTICAL AND ASTRONAUTICAL ENGINEERING

CARA L. WINTER, pp. 35–43
ENGINEERING MECHANICS

EDITOR: ERIC N. BROWN
DEPARTMENT OF THEORETICAL AND APPLIED MECHANICS
UNIVERSITY OF ILLINOIS AT URBANA-CHAMPAIGN
URBANA, IL 61801

CONFERENCE CHAIRS: KIMBERLY M. HILL AND JAMES W. PHILLIPS
DEPARTMENT OF THEORETICAL AND APPLIED MECHANICS
UNIVERSITY OF ILLINOIS AT URBANA-CHAMPAIGN
URBANA, IL 61801

ILLINOIS
1867
UNIVERSITY OF ILLINOIS AT URBANA-CHAMPAIGN

FOREWORD

The Undergraduate Research Conference in Mechanics is open to all UIUC undergraduates pursuing independent and faculty-supervised research on any topic in the mechanical sciences.

The conference is sponsored by the UIUC Department of Theoretical and Applied Mechanics and the Richard G. and Sandra S. Carlson Fund.

"*My wife, Sandra, and I believe strongly in supporting continuing education, both in engineering and the wider academic community. The future our state, country, and community depends on continued aspiration for excellence in the education of our youth. We actively champion improvements in educational programs at the university and high school level. It is our pleasure to nurture efforts in the TAM department such as the Undergraduate Research Conference. The conference provides an excellent addition to the undergraduate experience in mechanics.*"

—Richard G. Carlson, March 13, 2003, Conference Sponsor
TAM Alumnus (M.S. 1965, Ph.D. 1967)

"*The most important thing about doing research is the realization that there is exciting, unknown, but still accessible stuff that's being done all around you. I'm working on things that nobody else in the world is working on, things that could be in the next generation of software, and I'm sitting there in the midst of it.*"

—Ryan J. Giordano, 2002 UGRC first place winner, best project and best presentation
TAM Alumnus (B.S. 2002)

The papers in this volume were presented on April 25, 2003, at the University of Illinois at the Fifth Undergraduate Research Conference in Mechanics. The conference was organized by Prof. Kimberly M. Hill and Prof. James W. Phillips. The editor wishes to thank all the faculty members from various departments who advised the individual students and aided in the writing of these papers.

—Eric N. Brown, Editor
(Ph.D. 2003)

UNDERGRADUATE RESEARCH CONFERENCE AWARDS

The Theoretical and Applied Mechanics department awards prizes to recognize excellent projects and presentations. The recipients of the 2003 award for undergraduate research are:

Clarence E. Dienberg and Stephanie E. Ott-Monsivais.

EFFECTS OF AN UNDERBODY DIFFUSER ON AUTOMOBILE LIFT AND DRAG CHARACTERISTICS

Clarence E. Dienberg
Senior in Engineering Mechanics, UIUC
Kimberly M. Hill
Faculty Sponsor and Professor in Theoretical & Applied Mechanics, UIUC

Several technological developments that have improved racecar performance have begun to trickle down to passenger cars. The underbody diffuser is an example of a modification that greatly improves lift and drag characteristics of automobiles. The diffuser counteracts an inherit lift force that occurs on automobiles at high speeds, resulting in better handling and control. The configuration of the diffuser, however, is critical. The objective of this study was to examine the effect of the diffuser orientation on lift and drag coefficients as it varies with both wind speed and ride height. This was done using a simplified model car and a tabletop wind tunnel.

1. INTRODUCTION

Lowering lift and drag is one of the traditional goals of the auto industry. It is easy to see why this is true. Lowering drag increases fuel economy, lowers wind noise, and allows for higher top speeds and better acceleration. Reducing lift results in more secure high-speed handling. Due to limitations such as traditional styling [1], manufacturing processes, and industry trends, many restrictions are placed on the upper body design of modern automobiles. Therefore, in order to lower drag and obtain better lift characteristics, automobile manufacturers are focusing attention on the automobile underbody.

Of particular interest lately is the underbody diffuser. A diffuser is a device shaped to accelerate or decelerate a fluid. Low-velocity flows are associated with high-pressure and high-velocity flows with low-pressure. The diffuser in the experiment creates a high-velocity, low-pressure distribution along the bottom of the car underbody. This configuration can help produce a net downward force [2]. This diffuser, while seemingly simple in concept, is difficult to analyze because of the limited understanding in this area of nonlinear fluid mechanics. For example, drag on a cylinder for high velocity (high Reynolds number) flow is known experimentally, however, detailed analysis is lacking [2]. The complexity of the geometry also makes wind tunnel measurements and numerical simulations expensive and difficult to conduct [3]. The experiment described in the paper, which uses a simplified model car, was designed to measure the effect of a simplified diffuser. The experiment closely follows work by Cooper, Sovran, and Syms [4].

2. EXPERIMENTAL PROCEDURE

The simplified model car, shown in Figure 1, was developed in order to create a less complex problem and isolate the effects of the diffuser [2]. The rectangular boxed car was constructed with cardboard and duck tape due to time constraints and in order to facilitate modification. The car was 147 mm (5.8 inches) long, 53 mm (2.1 inches) high, and 55 mm (2.3

(a) (b)

Figure 1. Front of model car with sloped front configuration (a) and back of model car showing underbody diffuser at 18 degrees (b).

inches) wide. These ratios were taken from a typical full size car and scaled to fit the tabletop wind tunnel (manufactured by Klinger Educational Products). The front of the car had two configurations (see Figure 1): a flat front, similar to a diesel bus, or a sloped front, similar to a full size van. The cornered sides on the sloped front configuration (Figure 2a) were included to channel the flow of air over the *vehicle* and to ease modification of the diffuser angle and the front of the car. The back of the car was constructed to allow pieces to be added in order to close the gaps in the car, which would have otherwise let air in when the angle of the diffuser was changed. The diffuser, which measured approximately 25% of the length of the car, was hinged in order to allow for changes in the diffuser angle.

A diagram of the experimental setup is shown in Figure 2 to illustrate important variables. As shown in Figure 2, the drag force is parallel to the average direction of the wind. Lift is the force that is perpendicular to wind, and will be defined positive upward. The variable angle of the diffuser (θ) was measured as shown.

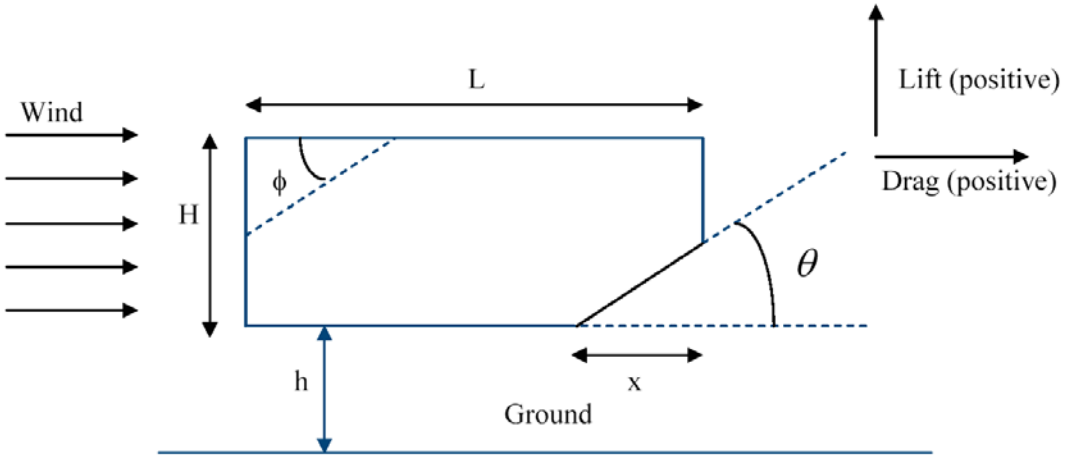

Figure 2. The Length of the car (L) was 147 mm (5.8 inches). The length of the diffuser (x) was 38 mm (1.50 inches). The variable angle of the diffuser (θ) ranged from 0 to 18 degrees in two-degree increments. The five ride heights (h) were 48 mm (1.88 inches), 38 mm (1.50 inches), 29 mm (1.13 inches), 19 mm (0.75 inches), and 10 mm (0.38 inches). The angle ϕ was either 35 degrees for the sloped configuration, or zero degrees for the flat front configuration. The height of the car (H) was 53 mm (2.10 inches).

The variable ϕ (approximately 35 degrees) was the angle of the front of the model car in the sloped (diesel bus) configuration. The length of the model car was L (147 mm, 5.8 inches) and x was the length of the diffuser (38.1 mm, 1.5 inches). Ride height (h) was the distance from the bottom of the wind tunnel to the bottom of the model car. The ride height is similar in concept to the ground clearance of a real automobile, however, due to the scaling from the real car to the model, a comparable h value would be too small to measure accurately.

The angle of the diffuser varied in two-degree increments from 0 to 18 degrees. The car was then placed in a tabletop wind tunnel as shown in Figure 3. For each diffuser angle, five ride heights (48 mm (1.88 inches), 38 mm (1.50 inches), 29 mm (1.13 inches), 19 mm (0.75 inches), and 10 mm (0.375 inches)) and four speeds (7.1 m/s, 9.3 m/s, 9.8 m/s, and 10.3 m/s) were measured. The average wind velocity was measured with a manometer as well as an electronic data acquisition system for time-averaged measurements [5]. A side velocity Profile of the wind tunnel is provided in Figure 3.

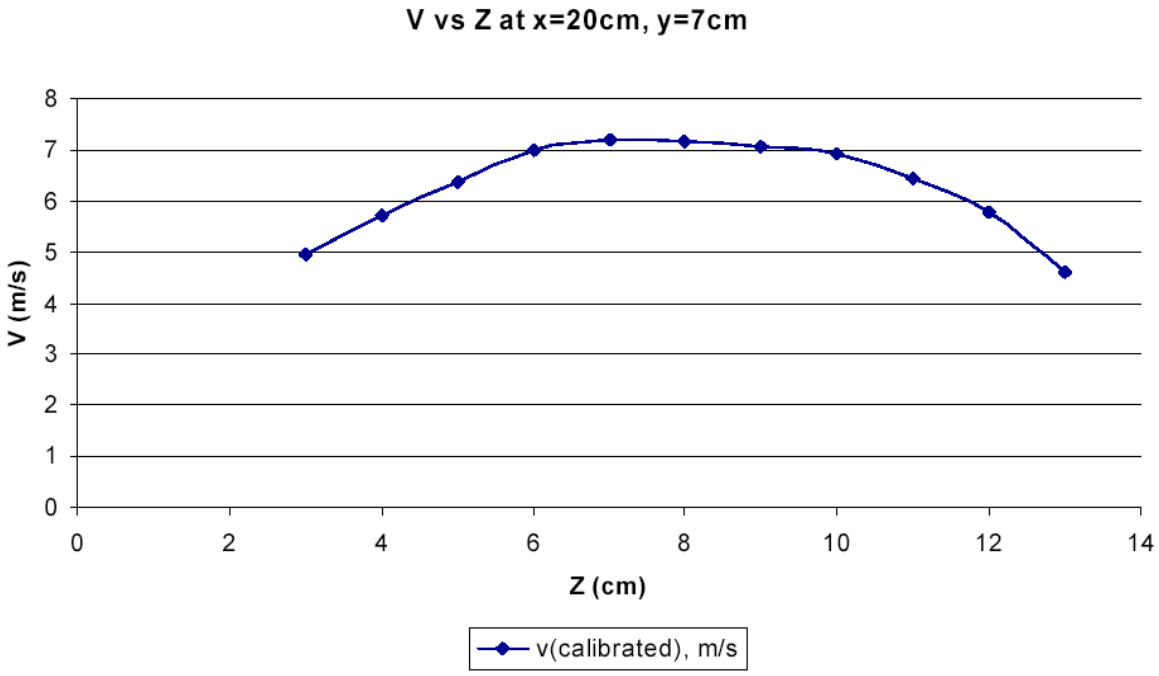

Figure 3. Side velocity profile of the wind tunnel.

For each diffuser angle, ride height, and fan setting the lift and drag on the model were measured using simple mechanical devices shown in Figure 4. The mechanical devices consisted essentially of a linear spring for the lift measurements (Figure 4c) and a torsional spring for the drag measurements (Figure 4d). After the measurements were taken, the car was removed from the wind tunnel and the diffuser angle was changed. The procedure was then repeated for all of the diffuser angles.

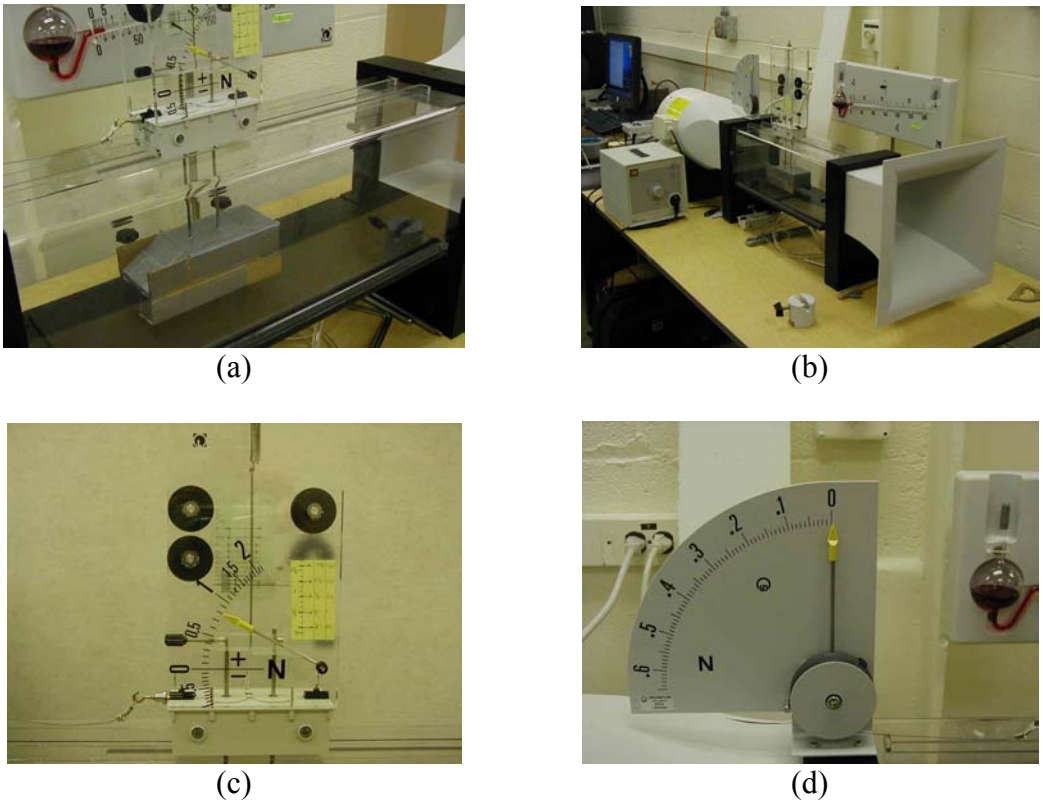

Figure 4. Tabletop wind tunnel set up (a and b). The measurements of lift and drag were obtained using mechanical devices consisting essentially of a linear spring for the lift measurements (c) and a torsional spring for the drag measurements (d).

3. RESULTS

Figures 5 through 8 show typical results from the experiment. The graphs selected were chosen for clarity of presentation, however all graphs in each category exhibited similar trends. Figure 5a shows drag as a function of ride height for different wind speeds for a diffuser angle of 8 degrees, but all other diffuser angles yield similar results. Figure 5a illustrates two trends; drag increased as the wind speed was increased and drag increased with decreasing ride height. Figure 5b shows the effect of diffuser angle on drag. As the angle of the diffuser increased, drag decreased. Even though Figure 5b is for a wind speed of 10.3 m/s, a similar trend was shown to hold for the other velocities in the experiment.

Figure 6 shows how lift decreased (i.e. more downward force) as the angle of the diffuser was increased. As the diffuser angle passed through approximately 6 degrees, the sign of the lift went from positive to negative. Figure 6 is for a wind speed of 9.8 m/s. Other wind speeds showed a similar trend, however the magnitude of the downward force becomes greater as the velocity was increased. An interesting trend in Figure 6 is that the lift decreased until an angle of 16 degrees is reached, at which point the lift started to increase. Sixteen degrees seemed to be a special angle, however further investigation showed that this trend is due to other factors, as will be discussed below. The effects of ride height on lift were inconclusive in the experiment.

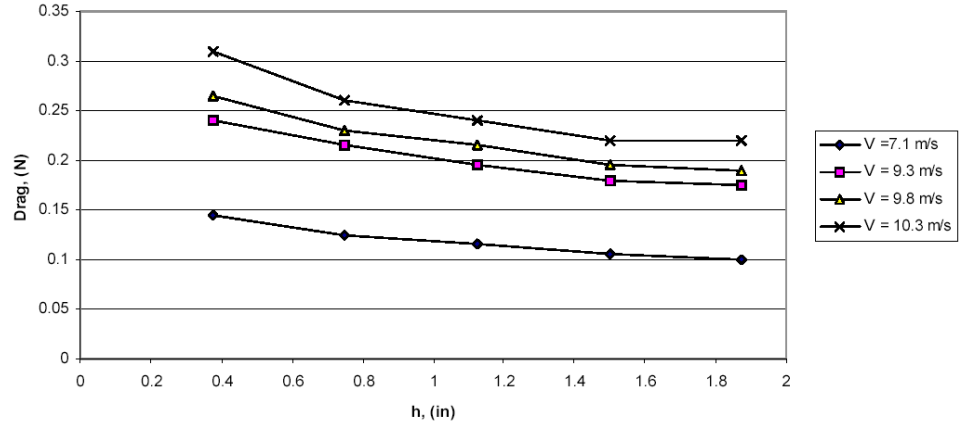

(a)

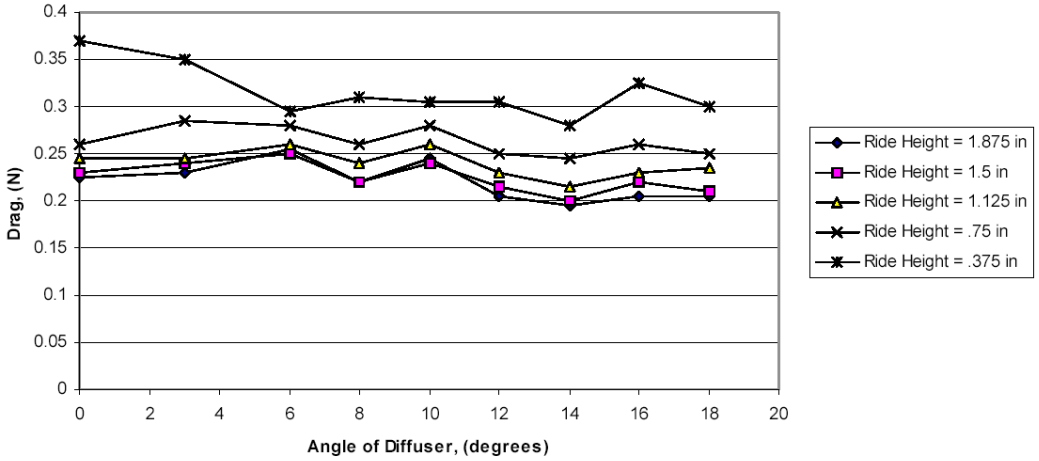

(b)

Figure 5. (a) Drag vs. ride height (h) for different wind speeds for a diffuser angle of 8 degrees, and (b) drag vs. angle of diffuser for different ride heights with a wind speed of 10.3 m/s.

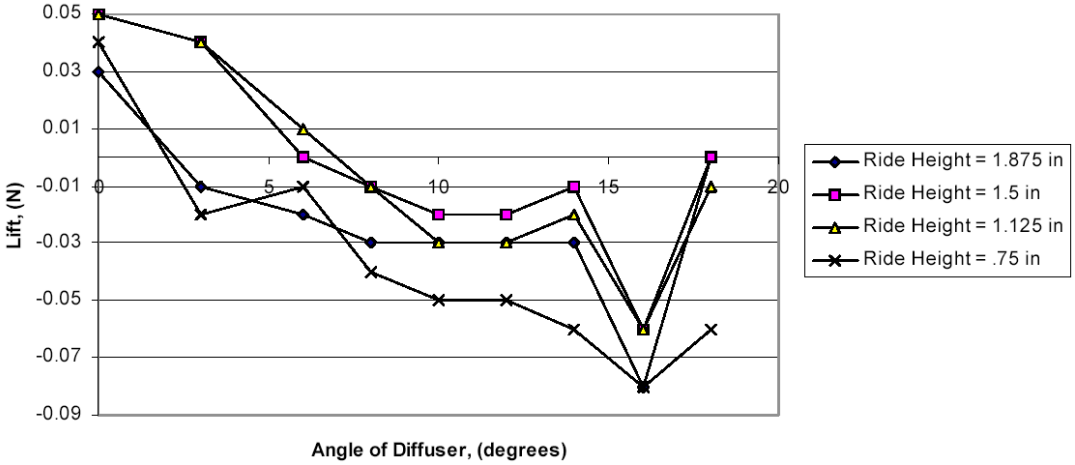

Figure 6. Lift vs. angle of diffuser for different ride heights with a wind speed of 9.8 m/s.

4. DISCUSSION

Some of the results mentioned above are intuitive, however some are not. First, as we might expect from everyday experiences, drag increased as the wind speed was increased (Figure 5a). This is particularly noticeable when walking or biking into the wind. For the situation at hand (velocities above 0.01 m/s), an approximation given by [6] concludes drag force is proportional to velocity squared. Drag also increased with decreasing ride height. This observation was less intuitive, and was most likely do to the complicated interaction between the bottom of the wind tunnel and the bottom of the model car. As Figure 5b shows, an increase in the angle of the diffuser lowered drag. This effect was not as prominent as the others in the experiment, and is not intuitive. More downward force was applied to the model car as wind speeds increased. This trend was also not intuitive and less prominent than other trends in the experiment.

4.1. SENSITIVITY TO DETAILS

Figure 6 raised many questions. Was 16 degrees the angle where lift once again changed signs from positive to negative? Was 16 degrees the angle that produced the maximum negative lift? It turns out that the configuration at 18 degrees was different from the other angles in the experiment. The original model car had a fixed piece in the back that was used to connect to the diffuser at an angle of 18 degrees. This fixed piece allowed no air into the inside of the model car. All smaller angles utilized the original 18 degree piece in the back as well as an additional piece that was added on to allow connection between the diffuser and the back of the model car (Figure 7). The results of this design were that ultimately 18 degrees was qualitatively different than the other angles in the experiment.

To test the effect this construction had on lift, a new back was added to the car so that measurements could be taken with the diffuser angle at 18 degrees and the back of the car consisting of two pieces. Figure 8 shows this slight change in the construction of the model car had a large effect on the results.

The results in Figure 8 are identical to those in Figure 6, except for the difference in lift measured at 18 degrees. When 18 degrees was constructed like the other angles, the trends in the graph changed from Figure 6 to those shown in Figure 8. These results showed that 16 degrees was not a special angle, but rather how susceptible this type of experiment was to small details. These conclusions show the experimental results are very sensitive to small fluctuations in the car design, so care needs to be taken in developing a reproducible testing model.

Figure 7. The figure on the left shows the 18 degree configuration. The figure on the right shows an angle of 14 degrees. Notice how the bold lined 18 degree back piece is still there, and the additional piece is added onto the original 18 degree piece in order to close gaps.

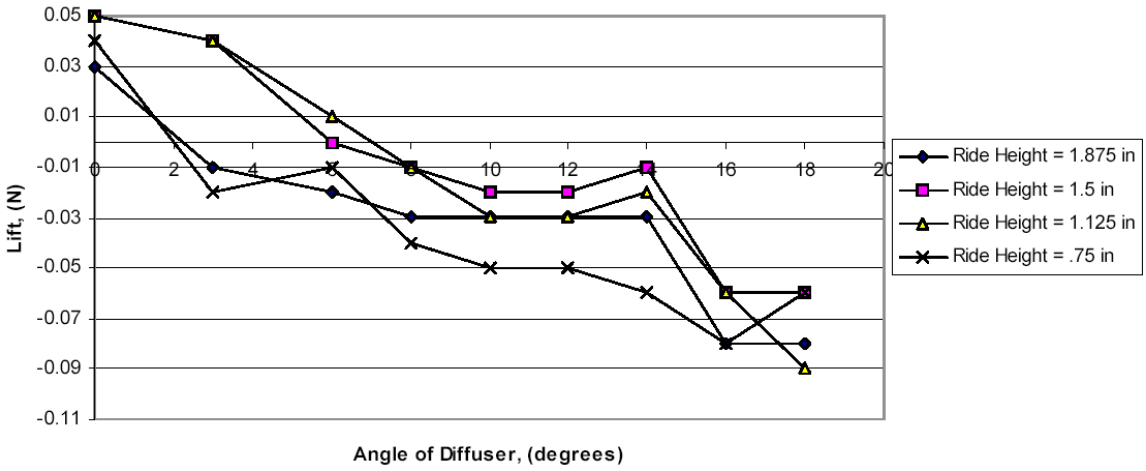

Figure 8. Lift vs. angle of diffuser for different ride heights with a wind speed of 9.8 m/s with new back piece.

4.2. WINDSHIELD (SLOPED FRONT) MODIFICATION

The measurements presented above were obtained using a flat front model car (no sloped front), which one could compare to a diesel bus. Data were also taken for a sloped front model car, which could be likened to a full size van. The trends of the results were the same overall, however adding the sloped front decreased drag and also increased negative lift. These results were expected, however, because the sloped front made it easier for the wind to pass over the front of the car resulting in less drag. The sloped front also created a force that generated a vertical component that increased negative lift (Figure 9).

The Reynolds number (Re) was calculated for the different wind speeds of the model car and for a real automobile at 24.6 m/s (55 mph). The Reynolds number was calculated using:

$$Re = \frac{\rho \times \upsilon \times l}{\mu}, \tag{1}$$

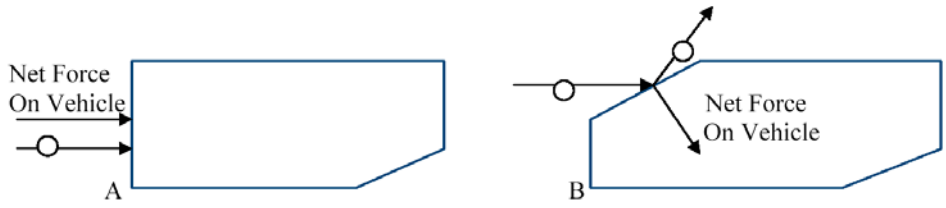

Figure 9. The circle represents an air particle. The net force on A (flat front model) was completely horizontal, while the net force on B (sloped front model) was split into vertical and horizontal components.

where the density of air ρ is 1.23 kg/m^3, the velocity of wind is υ, the characteristic length l is 0.146 m, and the viscosity of air μ is 1.79×10^{-5} N·s/m^2. Table 1 shows the Reynolds number corresponding to different velocities in the experiment. All of the *Re* numbers were in the moderate range, which resulted in complex flow behavior. Because the *Re* for the real car and the experimental setup were both in the moderate region, general similarities in behavior may be considered.

Table 1. Reynolds number for different wind speeds used in experiment and for a real car.

Wind Velocity (m/s)	*Re* [2]
7.1	1.7×10^4
9.3	9.3×10^4
9.8	9.8×10^4
10.3	10.3×10^5
Velocity of real car (i.e. relative wind velocity)	*Re* (with characteristic length of 4.14 m (163 inches))
24.6 m/s (55 mph)	7×10^6

5. CONCLUSIONS

Experimental studies were performed on a model car with an adjustable diffuser. It was found that negative lift increases with increasing angle of the diffuser. As the diffuser angle passed through approximately 6 degrees, the sign of the lift went from positive to negative. It was found that lift and drag increased with increasing wind speeds. Most likely do to the complex interaction between the bottom of the wind tunnel and the bottom of the car, drag increased as the ride height decreased. Minute details also had great effects on the experiment. Perhaps most significantly it was found that small changes in the physical construction of the car can have dramatic effects on the lift and drag forces. This was shown with a slight change to the back of the car and the corresponding changes in the trends that the new data presented.

In order to improve future experiments, materials other than cardboard should be used in the construction of the model car. Cardboard had an inconsistent surface finish, and the cutting and taping of the model did not allow perfect construction. An epoxy would be better for the application. Pressure taps should also be used throughout the surfaces of the car in order to integrate the pressure as a function of position. Pressure taps would allow for the use of analytical models that have been developed [2]. Finite Element Analysis, which is described in [1], [3], and [4], would also be a useful tool in analyzing the effects of the diffuser. Much more testing is needed in this area, and as automobile manufacturers start to use more underbody diffusers on their production cars, more testing of this phenomenon is likely to follow.

ACKNOWLEDGMENTS

We gratefully acknowledge the support of the Illinois Society of Professional Engineers (ISPE) funds for support of the equipment used for this project.

REFERENCES

1. D. Aronson, S. Brahim, and S. Perzon, 2000, On the underbody flow of a simplified estate. *Society of Automotive Engineers, Inc.*: 91–96
2. B. R. Munson, D. F. Young, T. H. Okiishi, 1998, Fundamentals of fluid mechanics, Third edition, John Wiley & Sons Inc..
3. S. Sebben, 2001, Numerical flow simulations of a detailed car underbody. *Society of Automotive Engineers, Inc*.: 167–173.
4. K. R. Cooper, G. Sovran, and J. Syms, 2000, Selecting automotive diffusers to maximize underbody downforce. *Society of Automotive Engineers, Inc.*, 47–61.
5. Cassy Software Version 1.3 by Leybold Didactic GMBH
6. G. R. Fowles and G. L. Cassiday, 1993, Analytical mechanics, Fifth edition, Harcourt Brace and Company.

STRUCTURE AND VELOCITY CORRELATIONS IN DENSE FREE SURFACE GRANULAR FLOW

Stephanie E. Ott-Monsivais
Freshman in Engineering Mechanics, UIUC
Kimberly M. Hill
Faculty Sponsor and Professor in Theoretical & Applied Mechanics, UIUC
Gustavo Gioia
Faculty Sponsor and Professor in Theoretical & Applied Mechanics, UIUC

When the slope of a sandpile is tipped beyond a critical angle (of about 30 degrees for dry particles) the grains of sand in a thin surficial boundary layer will begin to flow. Here, boundary layer granular flow was studied in a slowly rotated drum using different rotation speeds and bead sizes. A high-speed digital camera was used to locate and track the beads in the flowing layer. The results were used to obtain bead trajectories as well as average velocities and velocity fluctuation correlations as functionS of the depth across the flowing layer. The trajectories were used to show that the flowing layer is strongly stratified. The stratified structure of the flow was used as a basis for a simple model relating the velocity fluctuations to the structure of the flow.

1. INTRODUCTION

Granular materials are everywhere and the study of their flow can have numerous practical benefits. Most studies to date have focused on highly energetic, low-density granular flows, similar to a dense gas. (See, for example, Ref. [1].) The research described here focuses instead on dense granular flow, where the volume fraction approaches that of random close packing [2]. This type of flow is important geologically (e.g. in landslides) and industrially (e.g. in the transportation of grains, ores and powders) [3]. However, this flow is not well-understood; dense granular flow is very different from that of a conventional fluid in that granular flow is limited to a thin boundary layer [2, 4, 5].

The absence of a thorough understanding of dense granular flow reduces the efficiency of many industrial processes. Estimates show that even in the highly industrialized United States 60% of granular materials are wasted or contaminated in factories because of complications related to moving products from one part of an assembly line to another [3]. The lack of understanding of dense granular flow also impedes the prediction of natural disasters such as landslides. In the United States alone, landslides cause a minimum of $1.5 billion dollars in property damage, as well as incalculable personal suffering [3]. In summary, a better understanding of granular flow has significant potential practical benefit.

In the research described here, dense free surface boundary layer granular flow was studied experimentally in a slowly rotated drum for different rotation speeds and bead sizes. The results shed light on the structure of dense granular flow and were used to formulate a simple model relating the flow structure to the kinematics of the flow, in particular, to the correlation of the velocity fluctuations.

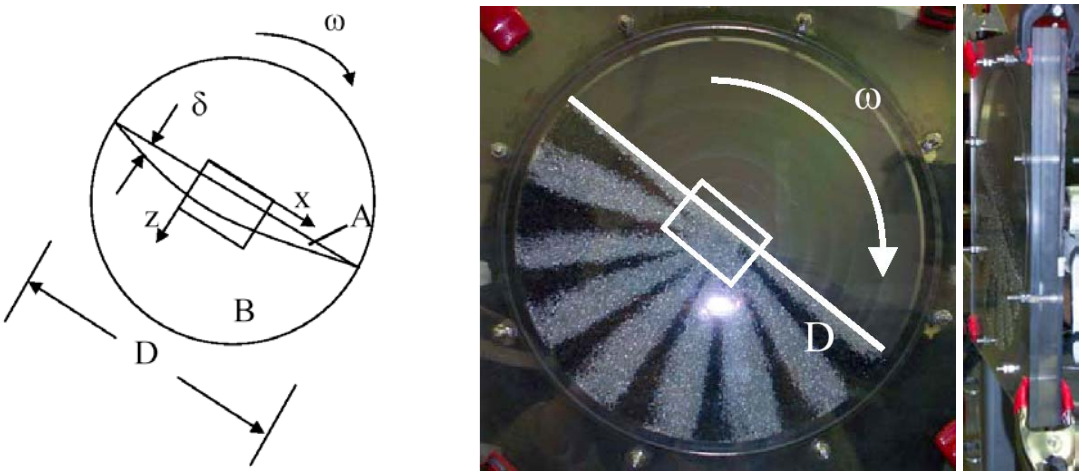

(a) (b)

Figure 1. (a) Schematic drawing and (b) photographs of the rotated drum with coordinate axes and thin surficial boundary layer (*flowing layer*) indicated in the drawing. The photograph to the right is a side view of the drum. The depth of the flowing layer is δ. In the flowing layer, the beads flow primarily parallel to the free surface. The drum is rotated slowly at a small angular velocity: ω. The boxed area shows the approximate area of the images obtained in the experiments.

2. EXPERIMENTAL PROCEDURE

For these granular flow experiments, a thin Plexiglas drum was partially filled with spherical plastic beads and rotated slowly about its axis. The beads used were either plastic or steel and either 2 mm or 3 mm in diameter (d). The drum was approximately 300 mm in diameter (D) and about 2.5 bead diameters deep. The drum was rotated at a constant angular velocity ω between 0.5 and 5 rotations per minute using a stepper motor (Compumotor). When the drum is rotated, only beads in a thin boundary layer (indicated with A in Figure 1a) actually *flow* (i.e., move relative to one another). Outside the flowing layer (indicated with B in Figure 1a) the beads rotate with the drum in a solid-like state.

Digital images were taken of the center of the flowing layer (See Fig. 1b) with a high-speed, high-resolution Photron Fastcam digital camera. A single experiment consisted of taking 1,024 images at 2 ms intervals. The resolution of the images was 1280 × 1024 pixels. A single video lighting source was used to illuminate the beads creating one reflection point on each bead (see Figure 2a).

A computer program [6] was used to locate each bead to within 1/100 of a bead diameter. The program was also used to remove artifacts such as that found in the upper left hand corner of Figure 2b. (For details, please see Ref. [6].) After locating all the beads in all the images, the same computer program was used to track each individual bead from image to image using a distance-minimization algorithm [6]. The resulting data was used to obtain individual bead trajectories, instantaneous velocity vectors (e.g., Fig. 3), average velocities (parallel and

perpendicular to the flowing layer), velocity fluctuations (parallel and perpendicular to the flowing layer), and velocity fluctuation correlations, as discussed below.

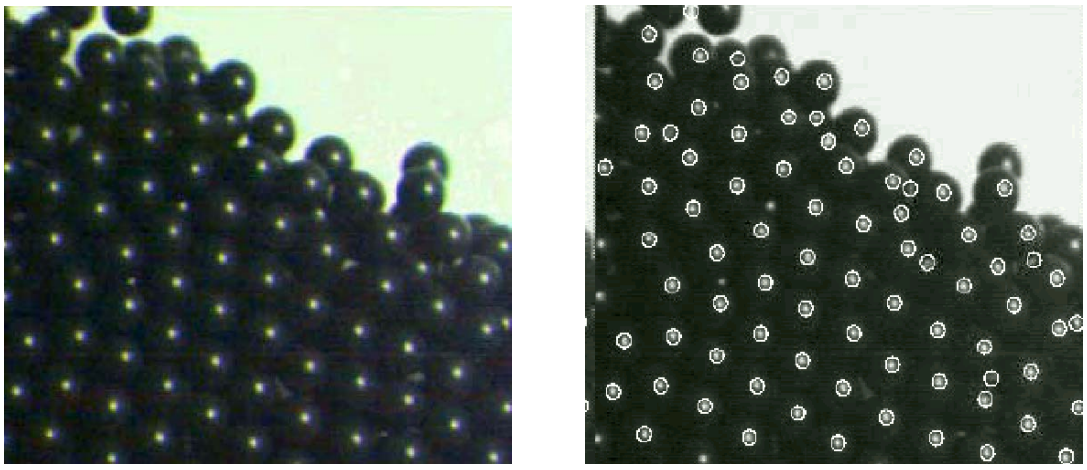

(a) (b)

Figure 2. (a) Because the beads are spherical and there is only a single light source, each bead has a single reflection point. (b) The image processing program [6] locates the reflection points on the beads and is later used to remove any stray and possible erroneous points.

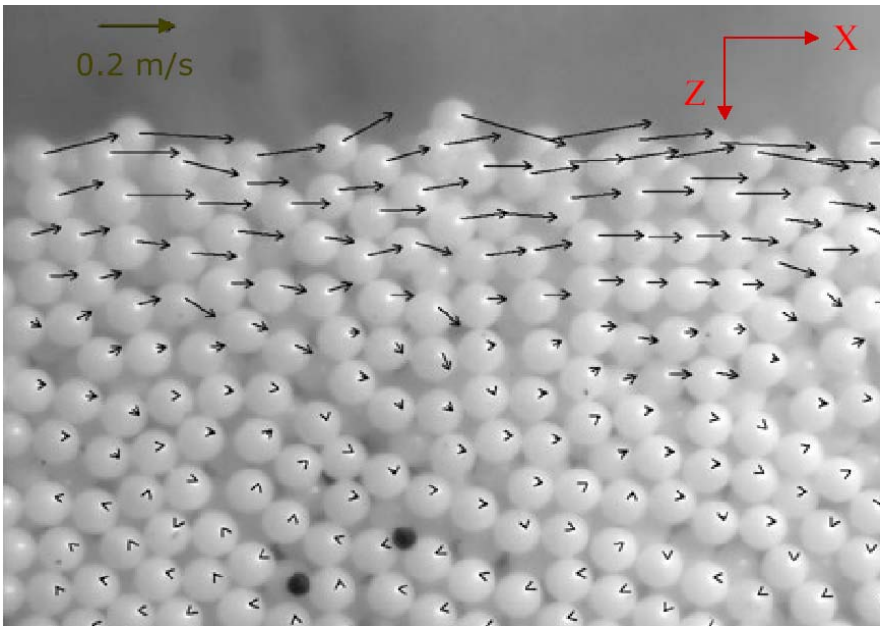

Figure 3. This is a picture of the flowing layer with overlaid instantaneous velocity vectors. Several qualitative details are apparent. For example, the velocity is primarily parallel to the free surface. It is greatest near the top of the flowing layer and then decreases to zero within about ten bead diameters from the free surface.

3. AVERAGE AND FLUCTUATING VELOCITIES

To compute the average velocity fields, each measured bead velocity was first corrected for the rotation of the drum as follows,

$$\vec{\mathrm{v}} = \vec{\mathrm{v}}_{measured} - \vec{\omega} \times \vec{r}\,, \tag{1}$$

where $\vec{r}$ is the distance from the center of rotation of the drum to the bead. Then, the corrected velocity was broken up into a component *v* perpendicular to the free surface and a component *u* parallel to the free surface as follows (Fig. 4):

$$\vec{\mathrm{v}} = u\hat{\mathrm{x}} + v\hat{\mathrm{z}}\,. \tag{2}$$

Figure 5 shows plots of v(t) and u(t) for an individual bead throughout one experiment, as well as the average velocities $\langle v \rangle = 0$ and $\langle u \rangle > 0$ (bold lines in Fig. 5). To calculate the average velocity fields, each frame from a single experiment was partitioned into bins of equal width, parallel to the free-surface boundary layer. The value of the mean velocity within a bin centered at a depth *z* (B_z) was calculated using the velocities of any bead with a portion of its volume in the bin:

$$\langle u \rangle_{B_z} = \frac{\sum_i \sum_b u_i^b V_i^b}{\sum_i \sum_b V_i^b}\,, \tag{4}$$

where the index *i* spans over all of the 1,024 images, and the index *b* spans over all the particles. In these equations, u_i^b denotes the instantaneous velocity of a bead *b* parallel to the free surface in the i^{th} frame, and V_i^b denotes the fraction of the volume of the bead *b* that falls within a bin centered at a depth *z* (B_z) in image *i* (Fig. 6). In order to obtain the mean velocity profiles, $\langle u(z) \rangle$, Equation (4) was applied to each bin across the boundary layer to obtain $\langle u \rangle_{B_z}$, and then the assignment $\langle u(z) \rangle = \langle u \rangle_{B_z}$ was made. For the graphs discussed below a bin size of $1/100^{\text{th}}$ of a bead diameter was used.

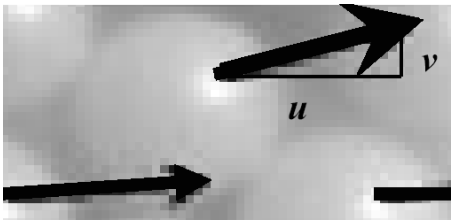

Figure 4. The net velocity of each bead is broken up into a component parallel to the free surface and a component perpendicular the free surface.

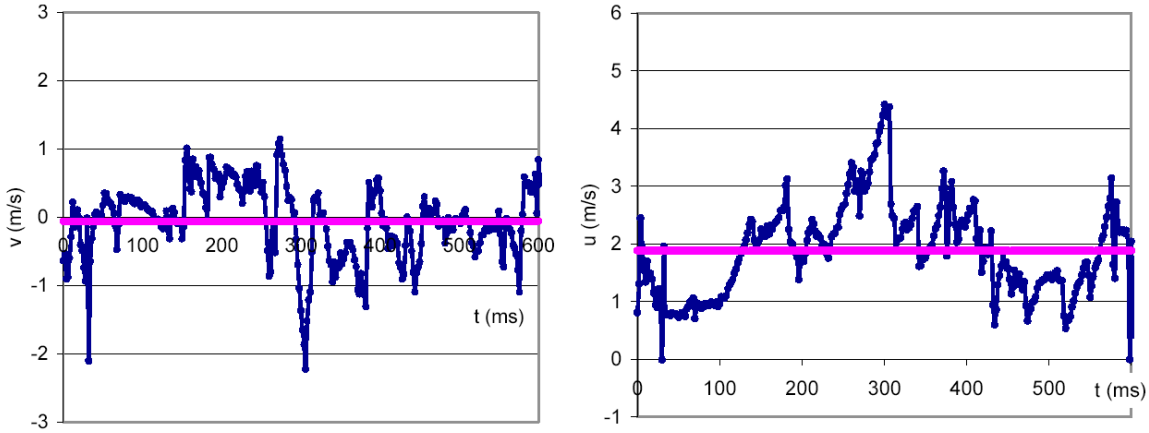

(a) (b)

Figure 5. (a) This is a plot of v (m/s) versus time (in ms) for an individual bead. The average value of v is zero (bold line). (b) This is a plot of u (m/s) versus time (in ms) for the same bead. The average value of u is about 2 m/s for this experiment (bold line).

The average velocities can be used to define the fluctuating velocities $v'(t)$ and $u'(t)$:

$$v'(t) = v(t) - \langle v \rangle = v(t), \text{ and}$$

$$u'(t) = u(t) - \langle u \rangle .$$

By definition, the average values of $v'(t)$ and $u'(t)$ are zero, $\langle v' \rangle = \langle u' \rangle = 0$. The fluctuating velocities may be characterized by computing the so-called velocity fluctuation correlations, $\langle u'u' \rangle$, $\langle u'v' \rangle$, and $\langle v'v' \rangle$. (These average fields are calculated in the same manner as described above and characterized by Equation (4).)

Section 4.1 is devoted to the study of the average velocities $\langle u \rangle$ and $\langle v \rangle$ as functions of the depth z (See Fig. 1a), whereas section 4.2 is devoted to the study of the velocity fluctuation correlations as functions of z.

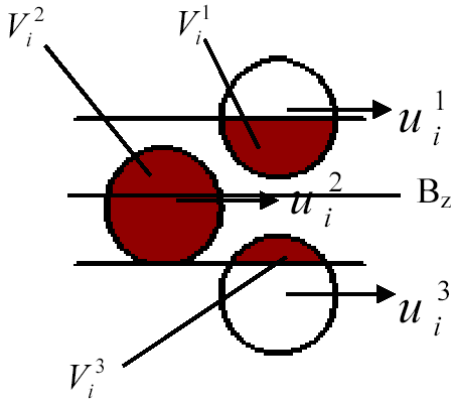

Figure 6. This diagram illustrates the method used to calculate the average fields.

4. EXPERIMENTAL RESULTS

4.1. AVERAGE VELOCITIES

Figure 7 shows plots of the mean velocity profiles $\langle u \rangle$ and $\langle v \rangle$ as functions of the depth z for beads of two different sizes (2 mm and 3 mm beads) rotated at two different angular velocities. The maximum value of $\langle u \rangle$ occurs near the free surface and then declines smoothly, vanishing at approximately 10 bead diameters below the free surface. As shown in Figure 7, when the angular velocity (ω) is increased both u_{max} and δ_{max} increase. If the bead size increases, u_{max} decreases and the depth of the flowing layer (δ) increases given that ω is held constant. (Note that in Figure 7 the depth is shown in bead diameters rather than in mm.)

4.2. VELOCITY FLUCTUATION CORRELATIONS

Figure 8 shows plots of $\langle u'u' \rangle$, $\langle u'v' \rangle$, and $\langle v'v' \rangle$ versus the depth z for a bead size of 2mm and for two different angular velocities of the drum. As was true for the velocities, the fluctuations are highest near the top of the flowing layer, and they increase with the speed of rotation of the drum. The results for the 3 mm beads are not shown, but their velocity fluctuation correlation graphs are similar to that of the 2 mm beads (Figure 7). As the bead size increases, the maximum velocity fluctuation correlations decrease, and the depth at which then correlations vanish increases.

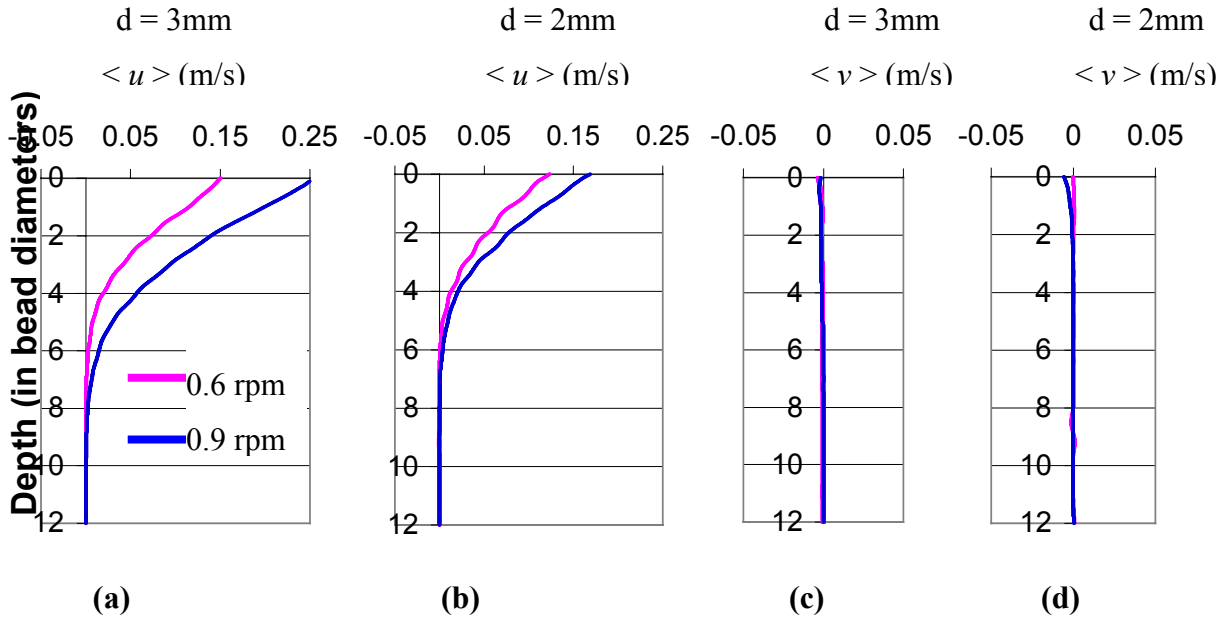

Figure 7. The mean velocity profiles for two different bead sizes and two different angular velocities, as indicated. (a) <*u*> versus z for d = 2 mm (b) <*u*> versus z for d = 3 mm (c) <*v*> versus z for d = 2 mm (d) <*v*> versus z for d = 3.

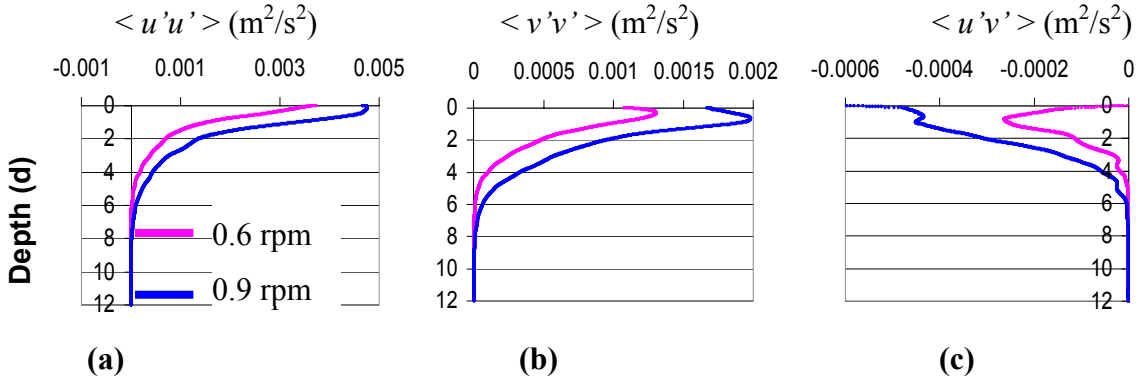

Figure 8. Velocity fluctuation correlations (a) $\langle u'u' \rangle$ (b) $\langle v'v' \rangle$ and (c) $\langle u'v' \rangle$ versus z for 2mm beads and at two different angular velocities, as indicated.

5. DISCUSSION – BEAD TRAJECTORIES AND FLOW STRUCTURE

In this section a simple model is developed that relates the velocity fluctuations to the average velocity parallel to the free surface $\langle u \rangle$ using the stratified structure of the flow reported in Ref. [2]. Figure 9 shows the trajectory of each bead from a single experiment superposed in a single image. This plot of the bead trajectories shows that most of the flow is stratified. In other words, the trajectories are grouped in bundles parallel to the flowing layer and at a distance of about one bead diameter from one another [3]. The beads appear to flow in lanes that are parallel to the free surface with some relatively small random movements perpendicular to the overall direction of the flow.

Thus at a given depth (i in bead diameters from the surface), one can consider a particular layer of beads to be stationary while the layer directly above moves with a relative velocity of the

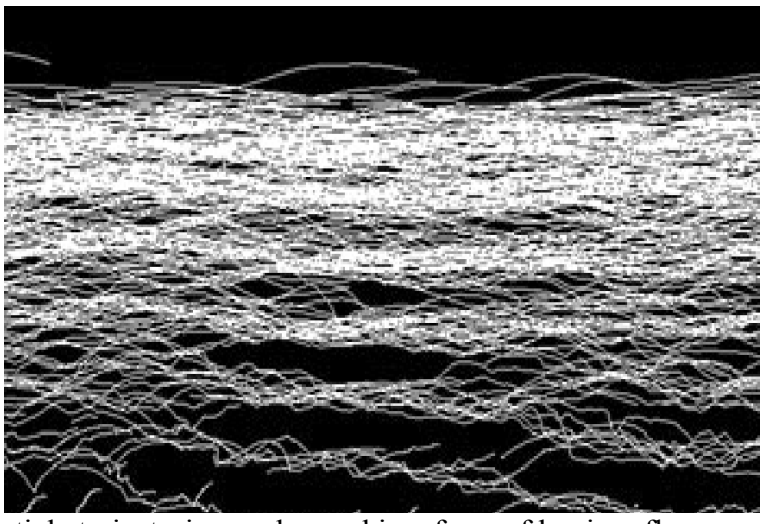

Figure 9. The particle trajectories are layered in a form of laminar flow.

difference between the velocity of these two layers. In other words, the average velocity of layer i relative to the layer $i+1$ immediately below $\langle u_{rel} \rangle$ can be written as

$$\langle u_{rel} \rangle = \langle u_i \rangle - \langle u_{i+1} \rangle, \tag{5}$$

where $\langle u_i \rangle$ is the absolute velocity of layer i and $\langle u_{i+1} \rangle$ is the absolute velocity of the layer $i+1$. Note that one can also relate the relative velocity to the shear rate $\dot{\gamma}$:

$$\langle u_{rel} \rangle = d\dot{\gamma}_i, \tag{6}$$

where d is the bead diameter. Imagine now a bead in layer i moving on the bumpy surface of layer $i+1$ (Fig. 10). Because of the bumpiness of layer $i+1$, the bead will oscillate up and down with a fluctuating velocity $v_i'_{rel}$ that can be modeled in the form:

$$v_i'_{rel} = A\cos(2\pi\dot{\gamma}_i t), \tag{7}$$

where A is the amplitude of the oscillation. The model approximates the relative movement of the bead as a sinusoidal path over the layer below (Fig.10). The amplitude should be proportional to the relative velocity between the two layers, so $v_i'_{rel}$ can be written in the form:

$$\begin{aligned} v_i'_{rel} &= \xi_v \langle v_{rel} \rangle \cos(2\pi\dot{\gamma}_i t) \\ &= \xi_v d\dot{\gamma}_i \cos(2\pi\dot{\gamma}_i t), \end{aligned} \tag{8}$$

where ξ_v is a dimensionless constant.

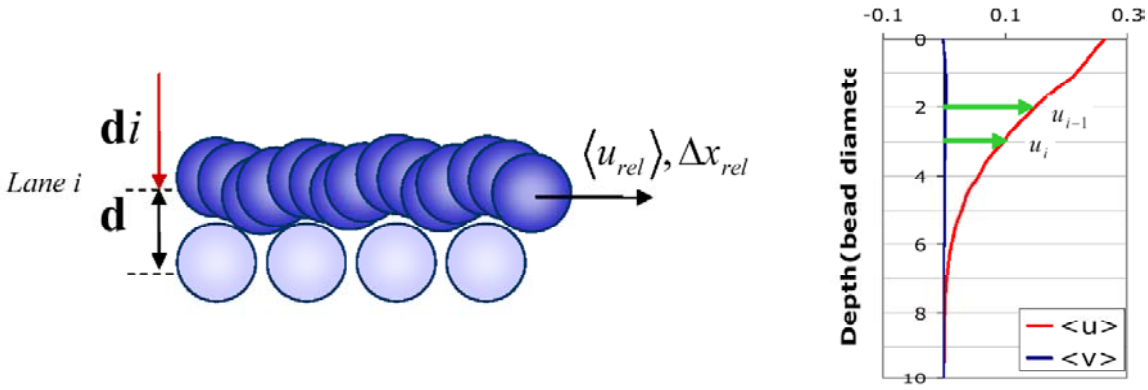

(a) (b)

Figure 10. (a) A bead moving relative to the layer below it. (b) Visual representation of average relative parallel velocity.

Similarly one can write

$$u_i'_{rel} = \xi_u d\dot{\gamma}_i \cos(2\pi\dot{\gamma}_i t + \phi), \tag{9}$$

where ξ_u is another dimensionless constant, and ϕ is a phase angle allowing for a phase difference between the fluctuations in the directions parallel and perpendicular to the top surface.

To derive expressions for the total velocity fluctuations, note that just as layer *i* moves relative to layer $i+1$, layer $i+1$ moves relative to layer $i+2$, and so on, to the bottom of the flowing layer. Associated with layer *i*, a sum must be performed over all the layers beneath layer *i* in the form:

$$v_i' = \sum_{j=\infty}^{i} \Delta v_j' = d\xi_v \sum_{j=\infty}^{i} \dot{\gamma} \cos(2\pi\dot{\gamma}t)$$

and

$$u_i' = \sum_{j=\infty}^{i} \Delta u_j' = d\xi_u \sum_{j=\infty}^{i} \dot{\gamma} \cos(2\pi\dot{\gamma}t + \phi). \tag{10}$$

The fluctuation correlation $\langle v'v' \rangle$ then follows as

$$\langle v'v' \rangle = \int v_i' v_j' dt = \int (d\xi_v)^2 \sum_i \sum_j \dot{\gamma}_i \dot{\gamma}_j \cos(2\pi\dot{\gamma}_i t)\cos(2\pi\dot{\gamma}_j t) dt. \tag{11}$$

Noting that $\int \cos(2\pi\dot{\gamma}_i t)\cos(2\pi\dot{\gamma}_j t) dt = \delta_{ij}/2$ where δ_{ij} is the Kroenecker delta function, this simplifies to

$$\langle v'v' \rangle = d^2 \xi_v{}^2 (0.5) \sum_{j=\infty}^{i} \dot{\gamma}_j{}^2. \tag{12}$$

Similarly,

$$\langle u'u' \rangle = d^2 \xi_u{}^2 (0.5) \sum_{j=\infty}^{i} \dot{\gamma}_j{}^2$$

and

$$\langle v'v' \rangle = d^2 \xi_u \xi_v (0.5) \cos\varphi \sum_{j=\infty}^{i} \dot{\gamma}_j{}^2. \tag{13}$$

These equations establish relationships between the shear rate $\dot{\gamma} = d\langle u \rangle / dz$ and each of the velocity fluctuation correlations $\langle u'u' \rangle$, $\langle v'v' \rangle$, and $\langle u'v' \rangle$. Because $\dot{\gamma}$, $\langle u'u' \rangle$, $\langle v'v' \rangle$, and $\langle u'v' \rangle$ have been caluclated from the experimental data as functions of z, the equations can be tested. Some results, shown in Fig. 11, demonstrate that the model works reasonably well for depths greater than approximately one bead diameter.

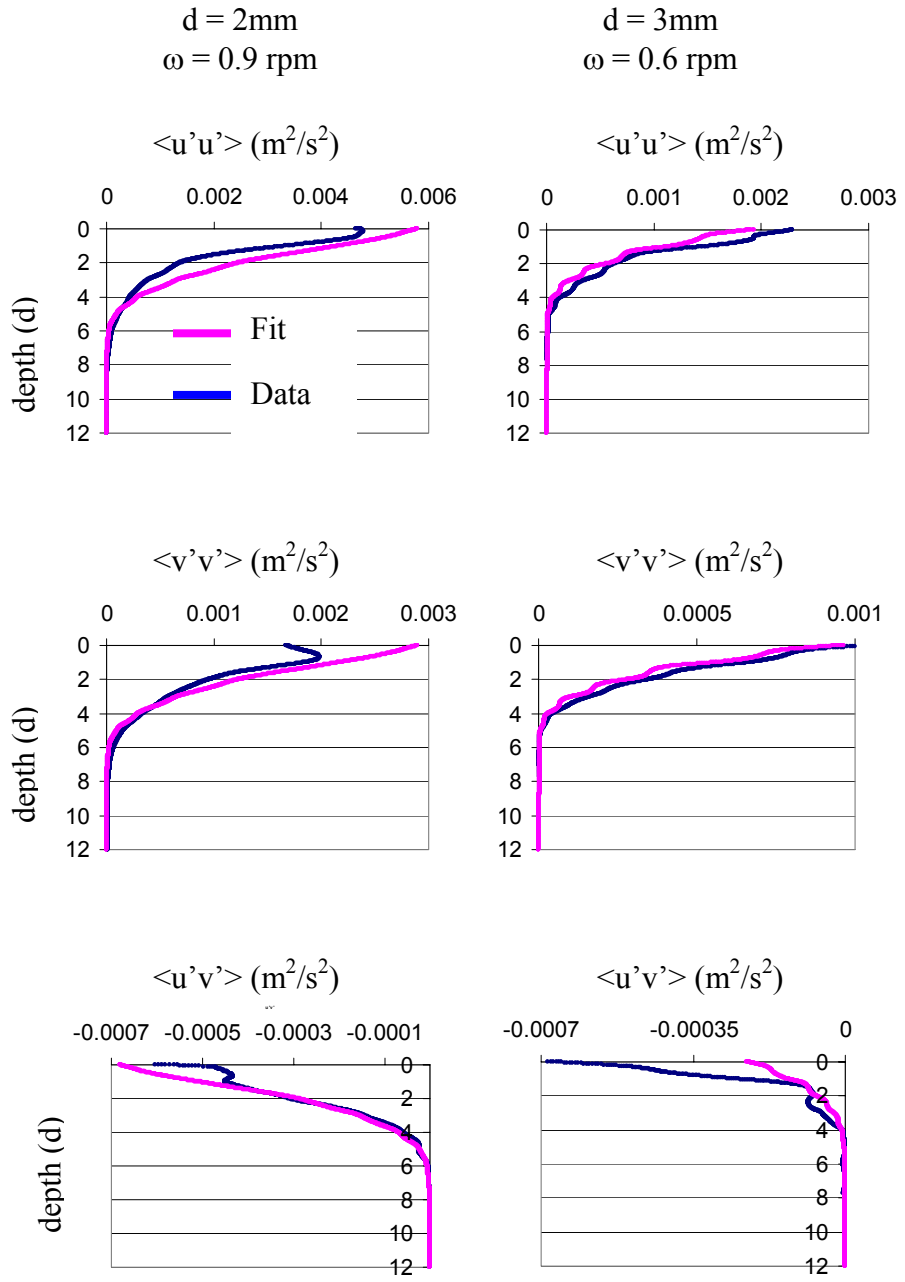

Figure 11. Using the same values $\xi_u = 1/10$, $\xi_v = 1/\left(10\sqrt{2}\right)$, and $\varphi = 98.5°$ to scale the model to the experimental data worked equally well for a variety of bead sizes and angular velocities. Here the results are shown for d = 2mm, ω = 0.9 rpm (first column) and d = 3mm, ω = 0.6 rpm (second column).

7. CONCLUSIONS

In this paper a dense free surface granular flow has been investigated by performing experiments in a rotating drum. By means of particle tracking it was possible to obtain the average velocity fluctuation correlations as functions of the depth across the flowing layer. It was also possible to obtain the particle trajectories and to use the particle trajectories to reveal the structure of the flow, which was shown to be layered parallel to the free surface. A simple model of the velocity fluctuations was proposed based on the layered structure of the flow. The predictions of the model were shown to be in good agreement with the experimental measurements.

ACKNOWLEDGMENTS

The UIUC Research Board and the UIUC Critical Research Initiative Program are gratefully acknowledged for their support of this research project.

REFERENCES

1. S. B. Savage, 1994, The mechanics of rapid granular flows. *Advances in Applied Mechanics* **24** 289-365 (1994).
2. K.M. Hill, G. Gioia, and V.V. Tota, 2003, Structure and kinematics in dense free-surface granular flow, *Physical Review Letters* **91**, 064302.
3. Carl Wassgren, Particulate Sciences Laboratory, http://widget.enc.purdue.edu/~psl/background/.
4. H.M. Jaeger, S.R. Nagel, R.P. Behringer, 1996, The physics of granular materials. *Physics Today* 32.
5. N. Jain, J.M. Ottino, R.M. Lueptow, February 2002, Physics of Fluids: An experimental study of the flowing granular layer in a rotating tumbler. *American Institute of Physics* **42**(2): 572–582.; D.M. Mueth, G.F. Debregeas, G.S. Karczmar, P.J. Eng, March 2000, Signatures of granular microstructure in dense shear flows, . Bonamy, R. Daviaud, L. Laurent, M. Bonetti, and J.P. Bouchaud, July 2002, Physical review letters: Multiscale clustering in granular surface flows. *The American Physical Society* **89**(3): 1–4.
6. The IDL and C++ program used to do many of the computations for this project was adopted from J.C. Crocker and E.R. Weeks. For additional information see http://glinda.lrsm.upenn.edu/~weeks/idl/tracking.html.

WAVE PROPAGATION AND VIBRATION BEHAVIOR IN CONCRETE

Joni L. Ranchero
Senior in Civil Engineering, UIUC
John S. Popovics
Faculty Sponsor and Professor in Civil Engineering, UIUC

Many non-destructive evaluation (NDE) techniques make use of mechanical waves (vibration and wave pulse propagation) to verify dimension, identify gross defects, and estimate strength of concrete. However, fundamental questions about wave propagation in concrete remain unanswered, especially with regard to the relation between wave propagation behavior and material properties. For example, differences between concrete Young's modulus derived from vibration, wave propagation and mechanical phenomena have been noted, although the reasons and precise nature of these differences are not clearly understood. A test series was carried out in order to shed light on these issues. A series of concrete test samples were subjected to wave propagation, vibration and mechanical tests, and material parameters (Young's Modulus, Poisson's ratio, density and P-wave velocity) are determined from each. The results are compared and the nature of the behaviors are analyzed. The differences in the observed behavior were interpreted with regard to two mechanisms; (i) differences owing to composite nature of the concrete and (ii) differences owing to the inherent mechanics of the tests (stress level, etc.). Preliminary conclusions regarding the relation between material properties and wave behavior are presented.

TENSILE PROPERTIES OF SELF-HEALING EPOXY

Alyssa A. Rzeszutko
Senior in Aerospace Engineering, UIUC
Eric N. Brown
Graduate Sponsor and Research Assistant in Theoretical & Applied Mechanics, UIUC
Nancy R. Sottos
Faculty Sponsor and Professor in Theoretical & Applied Mechanics, UIUC

This project investigates the effect of microcapsule concentration on tensile properties of self-healing epoxy. The self-healing material under investigation is an epoxy matrix composite, which incorporates microencapsulated healing agent that is released by crack intrusion. Polymerization of the healing agent is triggered by contact with an embedded catalyst. Uniaxial tensile tests were performed on standard dogbone samples to measure Young's modulus and ultimate strength. Both the modulus and ultimate tensile strength decreased with increasing capsule concentration. Moreover, recent testing revealed that the Young's modulus of self-healing epoxy at low concentrations of microcapsules, specifically from 0 to 30 wt%, decreased linearly. This behavior follows a rule-of-mixtures model assuming the microcapsules behave as voids.

1. INTRODUCTION

Thermosetting polymers are used in a wide variety of applications ranging from structural composites to microelectronics. Due to the low strain-to-failure exhibited by these polymers, they are highly susceptible to damage in the form of cracks. These cracks frequently initiate deep within a structure where detection is difficult and repair often impossible, ultimately leading to catastrophic failure. White et al. [1] have introduced a novel approach to recover the fracture properties of thermosetting polymers following crack propagation through the addition of self-healing functionality. Healing is achieved through the inclusion of urea-formaldehyde microcapsules that contain dicyclopentadiene (DCPD) healing agent. The composite with an initial crack is illustrated in Figure 1a. A propagating crack ruptures the microcapsules and exposes Grubbs catalyst particles embedded in the matrix. The opening of the crack draws the healing agent into the crack plane, exhibited in Figure 1b. Contact with the catalyst phase initiates polymerization, as shown in Figure 1c.

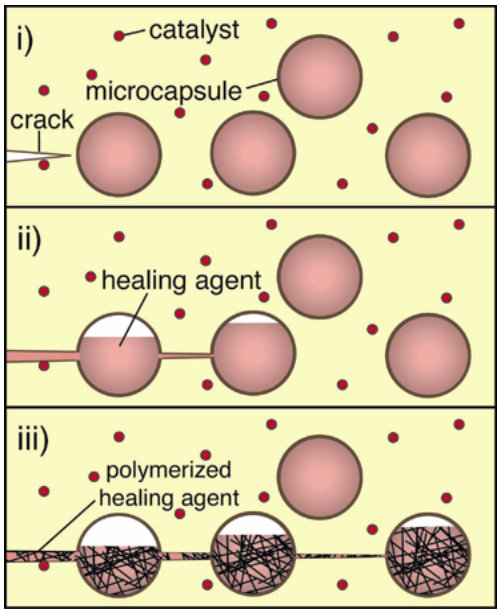

Figure 1. Crack propagation through a self-healing composite: i) crack initiation, ii) healing agent release, iii) polymerization of healing agent [1].

This self-healing material has been reported to recover up to 90% of its virgin fracture toughness [2]. Moreover, the inclusion of microcapsules increases the fracture toughness of the matrix material by up to 127% [3]. This paper investigated the effect of the microcapsules on the Young's modulus and ultimate stress of the composite material. Material properties were measured experimentally performing uniaxial tensile tests on dogbone samples [4] while incrementally increasing the amount of 180 μm diameter microcapsules added, from 0 to 30 wt%. A special consideration was made at 5 wt%, where two capsule sizes were tested (50 and 180μm). Micromechanical relationships as well as experimental studies [5] predict that the Young's modulus of the composite material will decrease with the volume fraction of the added filler if the modulus of the filler is lower than that of the resin.

2. EXPERIMENTAL PROCEDURE

Dogbone samples were manufactured from EPON® 828 epoxy resin (diglycidyl ether of bisphenol A, DGEBA) with 12 pph Anacmine® DETA (Diethylenetriamine) curing agent and with embedded microcapsules as outlined in Brown et al. [2]. Two microcapsule sizes (50 and 180μm average diameter) and incremental concentrations (0 to 30 wt%) were investigated. Microcapsule concentration defines the weight fraction of microcapsules in the self-healing polymer composite. The standard deviation for microcapsule diameter is less than 35% of the mean value over the two diameters investigated. Urea-formaldehyde microcapsules containing DCPD monomer were manufactured in-house, by the emulsion microencapsulation method [6]. Shell wall thickness of the urea-formaldehyde microcapsules ranges between 160 to 220 nm for both of the microcapsule diameters studied.

An aluminum mold was manufactured to make the silicon-rubber dogbone molds, as shown in Figure 2a and Figure 2b, respectively. EPON® 828 and Anacmine® DETA were first manually mixed together and then degassed to eliminate air pockets, or voids. The microcapsules were then manually stirred into the mixture. The three raw components of the mixture are shown in Figure 2c.

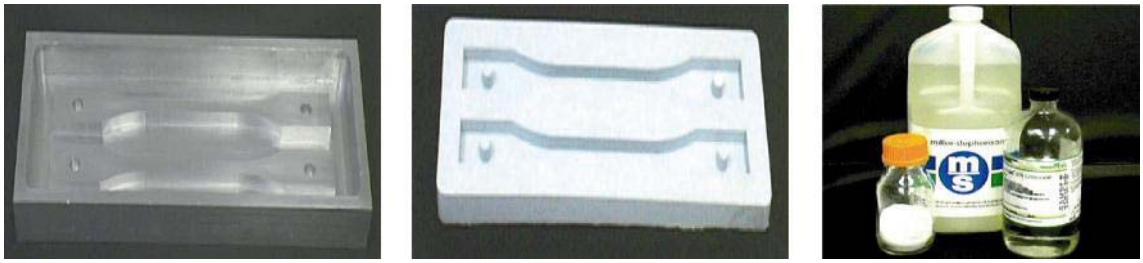

(a) (b) (c)

Figure 2. The molds to manufacture the samples and the ingredients: (a) aluminum mold, (b) silicon-rubber mold, and (c) mixture components.

As the amount of microcapsules added increased, the viscosity of the pre-cured mixture also increased. While stirring highly viscous batches, a second degassing procedure was necessary to remove any further air bubbles. The final mixture was poured into an open silicon-rubber dogbone mold. Occasionally, the vacuum chamber would fail to remove all of the

air bubbles. After pouring the mixture into the silicon-rubber molds, the air bubbles would rise to the top of the sample. A sharp toothpick was used to burst the remaining pockets of air. Removing all voids possible is necessary because a stress concentration is induced at the surface of the void location, and failure may occur at an artificially low load [7]. Steps of the manufacturing process are shown in Figure 3.

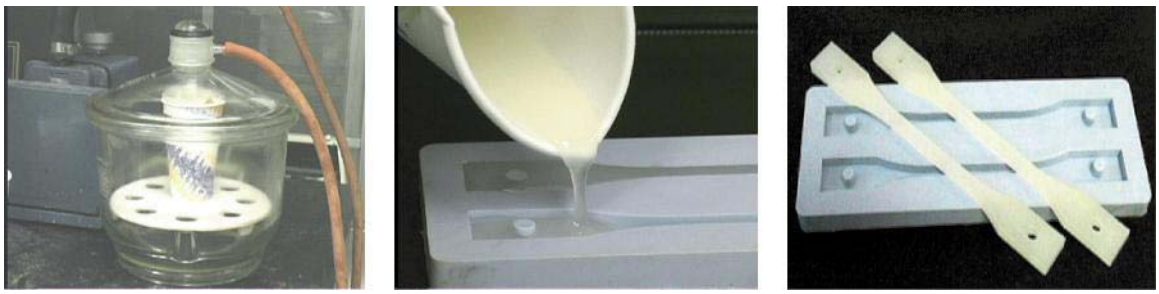

(a) (b) (c)

Figure 3. Steps of the manufacturing process in sequential order: (a) degassing, (b) pouring of mixture, and (c) cured specimens.

Samples were cured at room temperature for 24 hr followed by 24 hr at 30°C. Holes were cast in the samples to allow for pin loading in the Instron 8500 testing machine, as shown in Figure 4. The crosshead displacement rate was 0.05 mm s^{-1}. LabVIEW data acquisition software calculated values of engineering stress using the initial cross-sectional area. A clip-on extensometer was applied to the gage length of the dogbone specimen to measure strain. Values of the Young's modulus were calculated from a least-squares regression fit of the linear region of the stress–strain data, as shown in Figure 5. The last data point prior to fracture was recorded as the tensile strength, σ_{ult}.

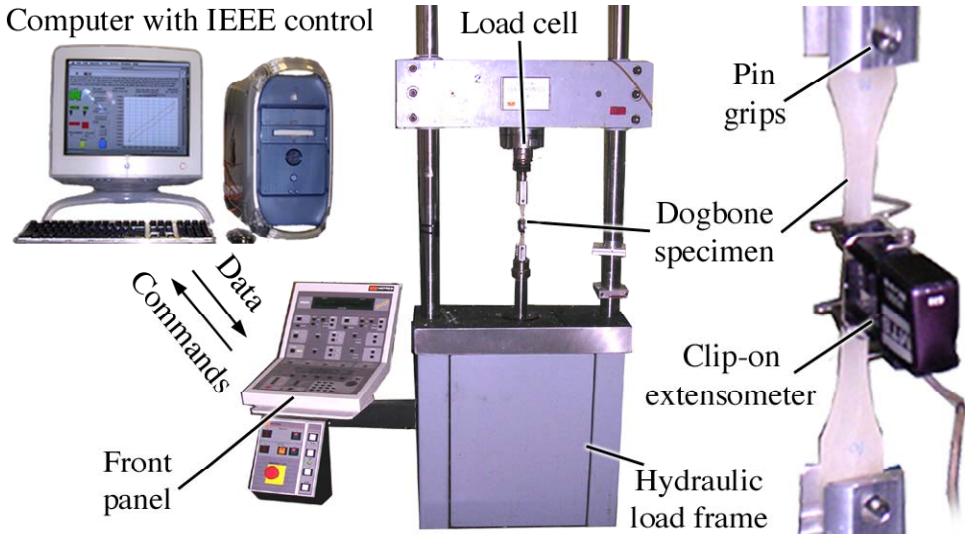

Figure 4. Instron hydraulic test frame with clip-on extensometer used to measure Young's modulus.

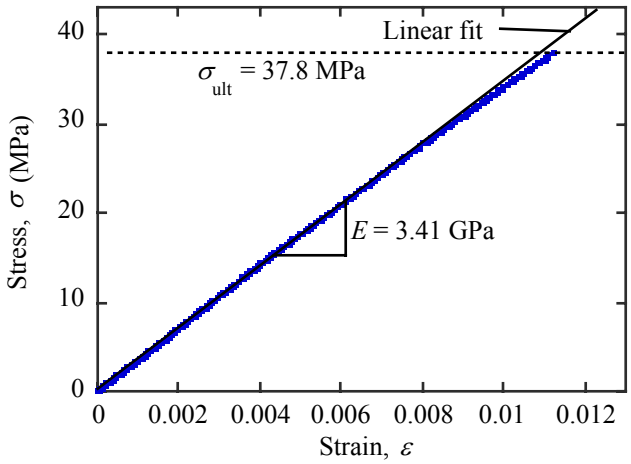

Figure 5. Representative stress–strain data for neat epoxy.

3. RESULTS AND DISCUSION

Each series of tensile specimens were tested to failure. Some of the samples failed at the grips rather than in the gage section. As expected with a brittle material, there was significant scatter in the ultimate tensile stress and strain data. However, the calculated Young's modulus of the material was more consistent within each volume fraction series. The data in Figure 6 show that the modulus decreases as the volume fraction of embedded microcapsules increases. The error bars in the figure are plus and minus one standard deviation. Each data point on the graph represents between 7 to 11 samples, where there is an average of 9.4 samples per data point.

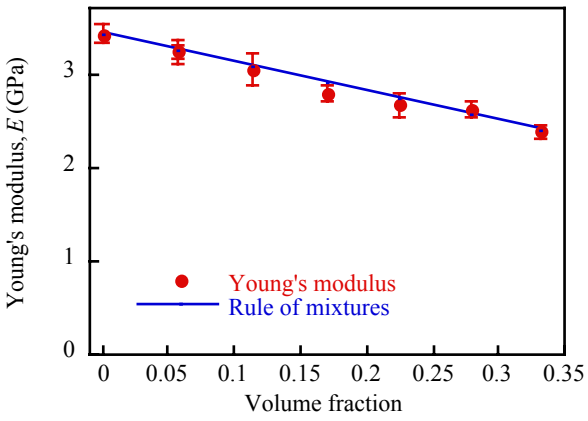

Figure 6. Young's modulus vs. volume fraction plotted against the rule-of-mixtures model.

If the microcapsules are assumed to have a negligible Young's modulus, such as a void, the behavior of the experimental data is captured exactly by the micromechanical rule-of-mixtures method [8]. The rule of mixtures is plotted in Figure 6 and given by

$$E_{\text{composite}} = V_{\text{microcapsule}}E_{\text{microcapsule}} + V_{\text{matrix}}E_{\text{matrix}} = V_{\text{matrix}}E_{\text{matrix}}, \quad (1)$$

where the $V_{\text{microcapsule}}$ and the V_{matrix} are the volume fractions of microcapsules and the matrix, respectively. The $E_{\text{microcapsule}}$ and the E_{matrix} are the Young's moduli of the microcapsule, and matrix, respectively. All samples were manufactured according to a pre-defined microcapsule weight increment (0 to 35 wt%). However, volume fraction is reported in Figure 6. The conversion from weight to volume fraction [8] is given by

$$V_{\text{microcapsule}} = \left[1 + \left(\frac{1}{w_{\text{microcapsule}}} - 1\right)\frac{\rho_{\text{microcapsule}}}{\rho_{\text{matrix}}}\right]^{-1}, \quad (2)$$

where $w_{\text{microcapsule}}$ is the weight fraction of the microcapsules (0.00 to 0.30). The density of the microcapsule, $\rho_{\text{microcapsule}}$, is approximately 1000 g/m^2. The density of the matrix, ρ_{matrix}, is approximately 1160 g/m^2.

The epoxy is nearly an ideal brittle material, exhibiting almost no ductility. The linear severity of each specimen's stress versus strain data prohibited the use of the 0.002 strain offset method to determine a yield stress value, σ_{YS}. Yield is a local phenomenon in these polymers. The yield stress is equivalent to the ultimate stress for every specimen. The load at which dogbone samples failed decreased significantly with the addition of microcapsules, as shown in Figure 7. Moreover, most of the neat epoxy and the 5 wt% samples failed in the gage length, while an increasing number of samples failed at the pin as the percentage of embedded microcapsules was augmented (Figure 8). The tensile strength of neat epoxy is 39 MPa, while the value for epoxy with microcapsules decreases to as low as 12 MPa for 30 vol% capsules.

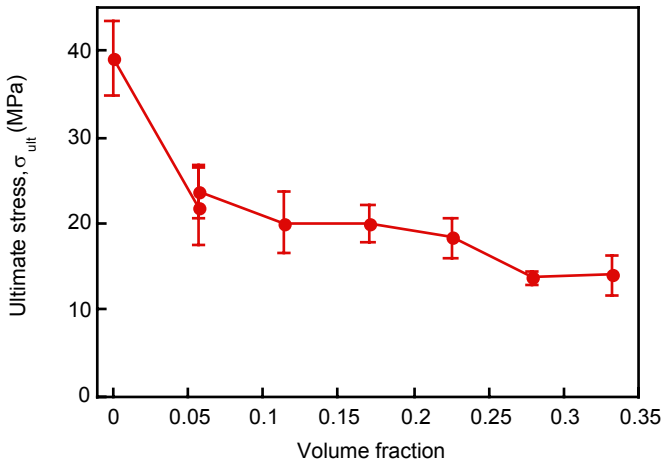

Figure 7. Ultimate stress vs. volume fraction of embedded microcapsules.

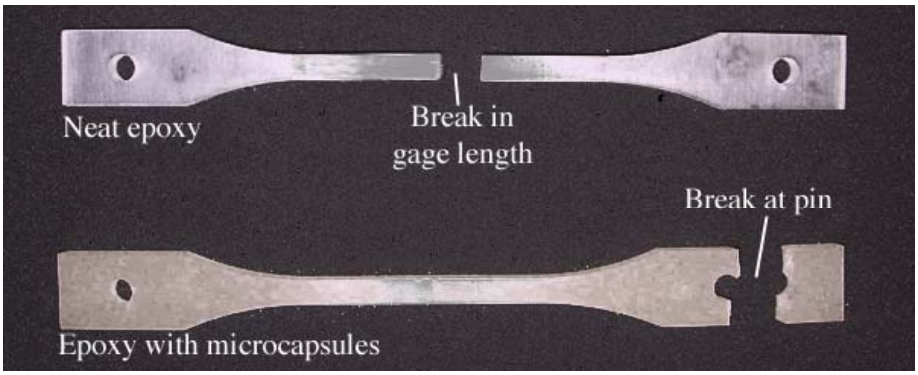

Figure 8. Break locations in dogbone specimens.

4. CONCLUSIONS

The effect on Young's modulus and ultimate stress of dogbone epoxy samples were studied under the incremental addition of embedded microcapsules. The samples underwent uniaxial-tensile tests. The viscosity of the pre-cured mixture increased with the addition of microcapsules. Elimination of air bubbles, or voids, in the samples became difficult, requiring a second degassing step in the manufacturing process. A void, if present, could introduce an increase in stress concentration at the void's location, possibly causing failure to occur earlier than expected. Both the Young's modulus and ultimate stress decreased as capsule concentrations increased from 0 to 30 wt%. In tension, the rule-of-mixtures model accurately captured the modulus data when the microcapsules were assumed to be voids. Two different sized diameter microcapsules, 50 and 180 μm, were tested at 5 wt%. Analysis confirmed that microcapsule size did not have a significant effect on tensile properties.

ACKNOWLEDGMENT

The authors gratefully acknowledge the support of the National Science Foundation, the AFOSR Aerospace and Materials Science Directorate Mechanics and Materials Program and Motorola Labs, Motorola Advanced Technology Center, Schaumburg Ill. The authors would also like to thank Dr. A. Skipor of Motorola Labs for technical support and helpful discussions. Mechanical testing was performed in the AMTEL facilities at UIUC with the help of Dr. P. Kurath and R. Rottet. Microcapsules were manufactured by M. Keller of the Autonomic Materials Group at UIUC.

REFERENCES

1. S.R. White, N.R. Sottos, P.H. Geubelle, J.S. Moore, M.R. Kessler, S.R. Sriram, E.N. Brown, and S. Viswanathan, 2001, Autonomic healing of polymer composites. *Nature* **409**, pp. 794–797.
2. E.N. Brown, N.R. Sottos, and S.R. White, 2002, Fracture testing of a self-healing polymer composite. *Experimental Mechanics* **42** pp. 372–379.

3. E.N. Brown, S.R. White, and N.R. Sottos, 2003, Microcapsule induced toughening in a self-healing polymer composite. *Journal of Materials Sciences* to appear.
4. ASTM Standard D 638-01. 2002. Standard test method for tensile properties of plastics. *Annual book of the American Society for Testing and Materials* (*ASTM*): *Plastics*. West Conshohocken ASTM: International. Vol 08.01:45–57.
5. R.L. Mccullough, 1990, Micro-models for composite materials—particulate and discontinuous fiber composites. Chapter in *Delaware Composites Design Encyclopedia*, Vol. 2*: Micromechanical Materials Modeling*. London: Technomic Publishing Co., Inc., 93–142.
6. E.N. Brown, M.R. Kessler, N.R. Sottos, and S.R. White, 2003, In situ poly(urea-formaldehyde) microencapsulation of dicyclopentadiene. *Journal of Microencapsulation* to appear.
7. M.M. Frocht, 1936, Photoelastic studies in stress concentration. *Mechanical Engineering* **58**, pp. 45–49.
8. B.D. Agarwal and L.J. Broutman, Analysis and performance of fiber composites. New York: John Wiley and Sons. 59–65

THE CHARACTERISTICS AND EVOLUTION OF STRIPED PATTERNS IN ROTATED GRANULAR MIXTURES

Cara L. Winter
Junior in Engineering Mechanics, UIUC
Kimberly M. Hill
Faculty Sponsor and Professor in Theoretical & Applied Mechanics, UIUC
Gustavo Gioia
Faculty Sponsor and Professor in Theoretical & Applied Mechanics, UIUC

Granular materials, such as powders and sand, tend to segregate due to differences in particle properties. In a dense flowing layer, small particles tend to sink, and large particles tend to rise. In a slowly rotated cylindrical drum partially filled with both small and large particles, this leads to a semi-circular radial segregation pattern, in which the smaller particles concentrate near the center of rotation and the larger particles concentrate near the outside walls of the drum. For fill levels of the drum close to 50% the radial segregation further develops into a striped pattern in which distinct stripes of the smaller particles spread toward the outer walls of the drum. If the speed of rotation of the drum is increased, the number of stripes decreases. In this paper, we study these phenomena experimentally and show that they may be explained with a simple model of the sheared interface between the two types of particles in the flowing layer.

1. INTRODUCTION

Mixtures of granular materials tend to segregate when shaken or otherwise disturbed. In nature, granular segregation might explain why the gravelly bed of a piedmont stream is frequently topped with a self-organized, stabilizing armour layer composed of the larger rocks in the bed. Granular segregation also occurs in many industrial processes, usually with undesirable effects. For example, segregation is a problem in the pharmaceutical industry, where the components of pills must be well mixed to ensure uniform distribution of medication. Understanding the mechanisms of granular segregation would allow us interpret related phenomena observed in nature and to prevent problems associated with many industrial processes.

Granular segregation has frequently been studied using a rotating drum (Figure 1a). When a granular material is rotated slowly in a drum, the particles flow (i.e., they move relative to each other) only in a thin surficial layer – the *flowing layer* (marked A in Figure 1a). Outside the flowing layer, in the region marked B in Figure 1a, the beads move in solid-like rotation with the drum. The flowing layer exchanges beads with the underlying substratum through the shallow arc PMQ of Fig. 1b. The beads positioned along the arc PM can be said to be *thawing* as they enter the flowing layer (and cease to move in solid-like rotation with the drum). Thus we can call PM the *thawing arc*. Similarly, the beads positioned along the arc MQ can be said to be *freezing* as they exit the flowing layer (and begin again to move in solid-like rotation with the drum). Thus we can call MQ the *freezing arc*.

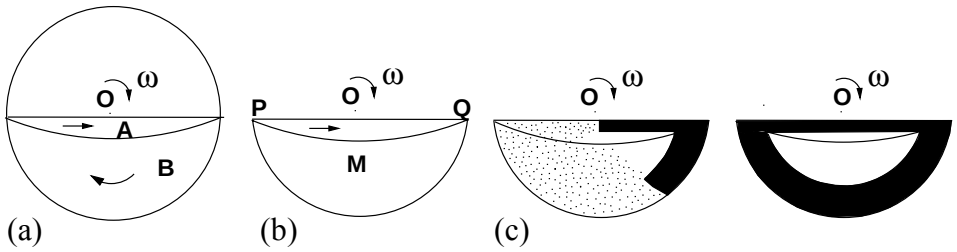

Figure 1. (a) Sketch of the drum. (The free surface is shown horizontal.) A is the thin flowing layer, B is the frozen substratum, and ω is the angular velocity. (b) Illustration of the freezing and thawing arcs (see text). (c) and (d) Cartoon of the formation of a semi-circular radial segregation pattern. (See text.)

Consider now the cartoon of Figure 1b-d. Because the black beads and white beads are initially well mixed, they enter the flowing layer through the thawing arc in a flux of constant composition (i.e., in a flux whose average composition is constant in time, Fig. 1b). As they move in the flowing layer, the larger, black beads segregate to the upper part of the layer and the smaller, white beads segregate to the lower part. Later, when these beads start to leave the flowing layer through the freezing arc, they begin to form a semi-circular radial segregation pattern (Fig. 1c). Last, when the beads frozen in the partially formed pattern reenter the flowing layer (again in a flux of constant composition), the semi-circular pattern becomes complete (Fig. 1d). In experiments, semicircular radial segregation patterns are observed to form just as in Figs. 1b-d, that is to say, within one rotation of the drum and for all fill levels. (See, for example, Refs. [1–3].) Figures 2a, b, and c show experimental results which correspond roughly to Figs. 1.b, c, and d, respectively.

For most fill levels, this semi-circular radial segregation pattern persists as the drum continues to rotate. However, when the fill level is near 50%, the semi-circular radial segregation does not remain steady [4]. Instead, the pattern evolves into a striped segregation pattern (Fig. 2.d). In a recent paper [5], it was studied why the striped segregation patterns form only in a narrow range of fill levels close to 50%. Here, we limit our studies to fill levels in that range and investigate how the striped segregation patterns evolve starting from semi-circular patterns and how the number of stripes varies with the angular velocity of the drum.

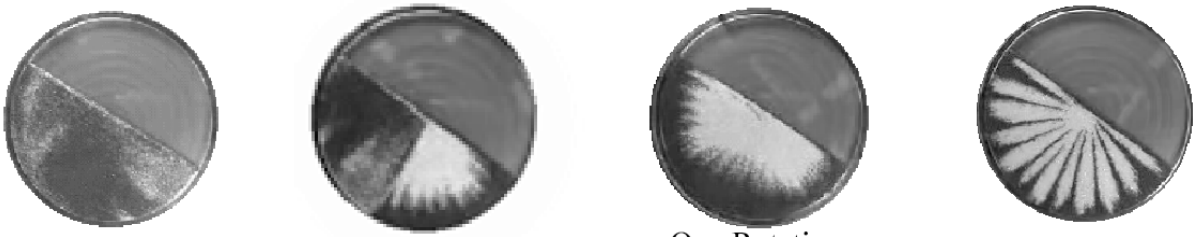

Figure 2. Experimental observations of granular segregation patterns in a ~50% full rotating drum. (a) Photograph of the initial condition: the small (white) and large (black beads are well mixed. (The large beads are black and small beads are white.) (b) Photograph of a partially formed semi-circular radial segregation pattern. (c) Photograph of a complete radial segregation pattern. (d) Picture of a striped segregation pattern.

2. EXPERIMENTAL PROCEDURES

In our experiments we rotate a cylindrical drum partially filled with a mixture of glass beads of two different sizes (Fig. 1a). The mixture consists of black beads with a diameter of 2mm (40% by weight) and white beads with a diameter of 0.8 mm (60% by weight). The drum has a diameter of ~300 mm and a thickness (perpendicular to the drawing in Figure 1a) of ~6.4 mm.

Throughout the experiments, we rotate the drum at a constant angular velocity (ω in Figure 1) that varies from experiment to experiment between 0.45 to 5.4 revolutions per minute (rpm). We control the angular velocity with a stepper motor (Compumotor) and take digital pictures at regular intervals in time during each experiment using a digital camera (Cohu) and a frame grabber board (Scion LG3).

3. EXPERIMENTAL OBSERVATIONS ON STRIPED PATTERN FORMATION

Figure 3 shows the evolution of the striped pattern starting from the semi-circular segregation pattern when the fill level of the drum is slightly more than 50% and $\omega = 0.45$ rpm. (The results are qualitatively similar for different mixtures, at other fill levels close to 50%, and for other angular velocities.) Figure 3a shows the same semi-circular radial segregation pattern

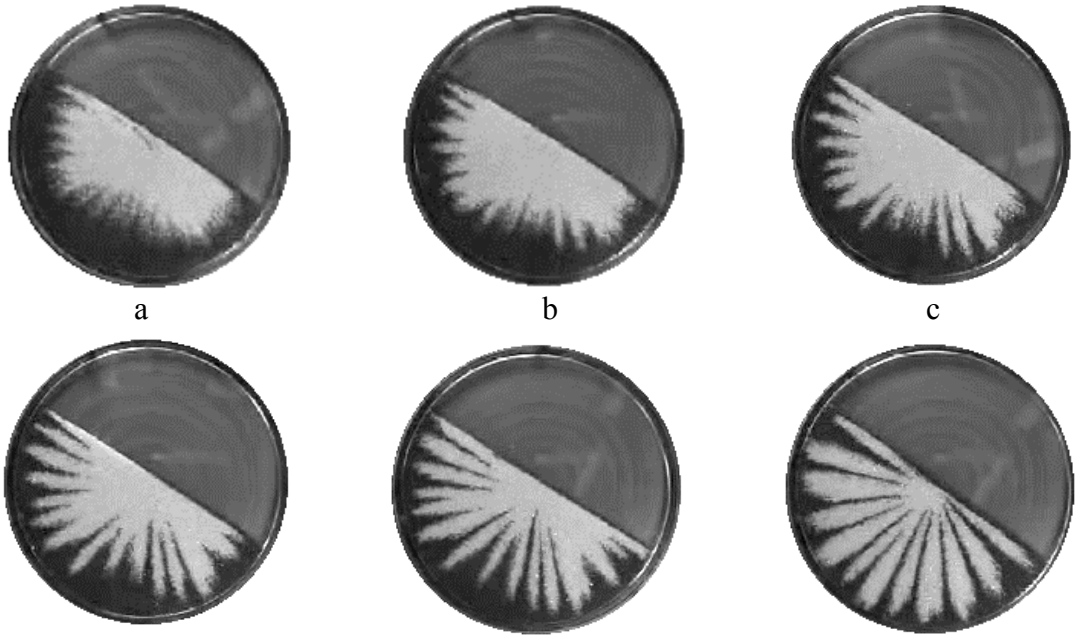

Figure 3. This shows the development of the striped segregation pattern from a radial segregation pattern. (a) A photograph of the semi-circular radial segregation pattern formed after one rotation. (b)-(e) Photographs of the pattern taken after two, three, four, and five rotations, as the striped segregation pattern evolves. (f) A photograph of the pattern after ten rotations, when the striped pattern has become steady.

as Fig. 2c. Note that the edge of this pattern is slightly *wavy*. If the drum rotates further, this waviness becomes amplified (Fig. 3b), leading to the development of a striped segregation pattern (Fig. 3c-e). With continued rotation, the segregation pattern reaches a steady state (Fig. 3f).

4. DISCUSSION

Consider the idealized semi-circular radial segregation pattern of Fig. 4a. In this pattern, the flux of beads entering the flowing layer through the thawing arc is of constant composition. That is to say, the rate at which both the small and the large beads enter the flowing layer is steady. Under these idealized conditions, the semi-circular radial segregation pattern may persist in time as the drum rotates. To see this, let us focus on the small portion of the boundary layer boxed in Fig. 4a. The flowing layer is segregated parallel to the free surface with the larger beads concentrated in the upper portion of the flowing layer and the smaller beads concentrated in the lower portion of the flowing layer (Fig. 4b). The velocity in the flowing layer decreases from top to bottom as sketched in Fig. 4b. (The measured velocity field is shown in Fig. 4c.) All these velocities are parallel to the free surface and therefore also parallel to the interface between the large and small beads. Because the velocity at the interface is parallel to the interface itself, the interface remains unaffected by the flow and therefore invariant under the idealized conditions of Fig. 4a.

The experiments of section 3 indicate that in actuality the semi-circular radial segregation pattern is not geometrically perfect as in Fig. 1d, but instead it is slightly wavy as in Fig. 3a. Because of this slight waviness, the flux of beads entering the flowing layer through the thawing arc is no longer of constant composition. Instead, the percentage of large beads entering the flowing layer

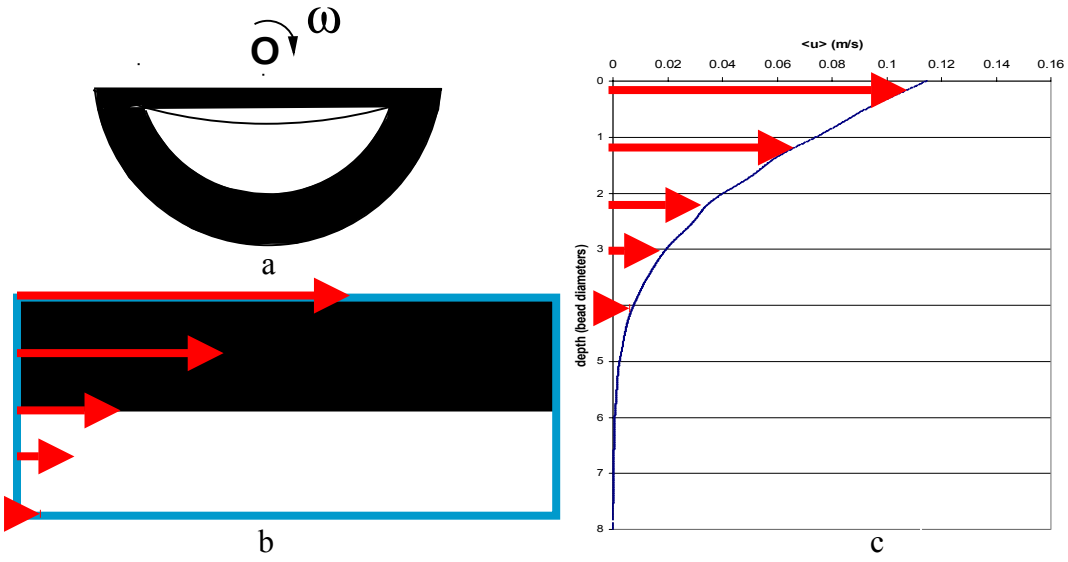

Fig. 4 (a) Illustration of an idealized semi-circular radial segregation pattern. (b) Detail of the small portion of the flowing layer boxed in 4a showing the horizontal interface between small and large beads. The arrows indicate the velocity at five different depths within the flowing layer. (c) Measured velocity field.

increases and decreases periodically in time (and the same is true of the percentage of small beads). Therefore, the interface between the small and large beads does not remain parallel to the free surface. Instead, the slope of the interface alternates between a positive value when the percentage of large beads is increasing in time (Fig. 5a) and a negative value when the percentage of large beads is decreasing in time (Fig. 5b). Because the velocity is always parallel to the free surface, it is clear in both Fig. 5a and Fig. 5b that regardless of the sign of its slope, the interface is not parallel to the velocity. Furthermore, because the velocity changes with depth, the interface may be advected resulting in an evolving interface.

Figure 5c shows a sketch of how the interface of Fig. 5a evolves. In this case, we can roughly say that the slope of the interface becomes less and less steep as the interface is advected by the velocity field. Figure 5d shows a sketch of how the interface of Fig. 5b evolves. In this case, a phenomenon that we can term *wave breaking* occurs, whereby the upper portion of the interface, advected at a higher velocity, overtakes the lower portion of the interface. The upper portion of the flowing layer is projected forward eventually to be frozen into an amplified stripe. The wave breaking is clearly apparent in the sequence of photographs of Fig. 6.

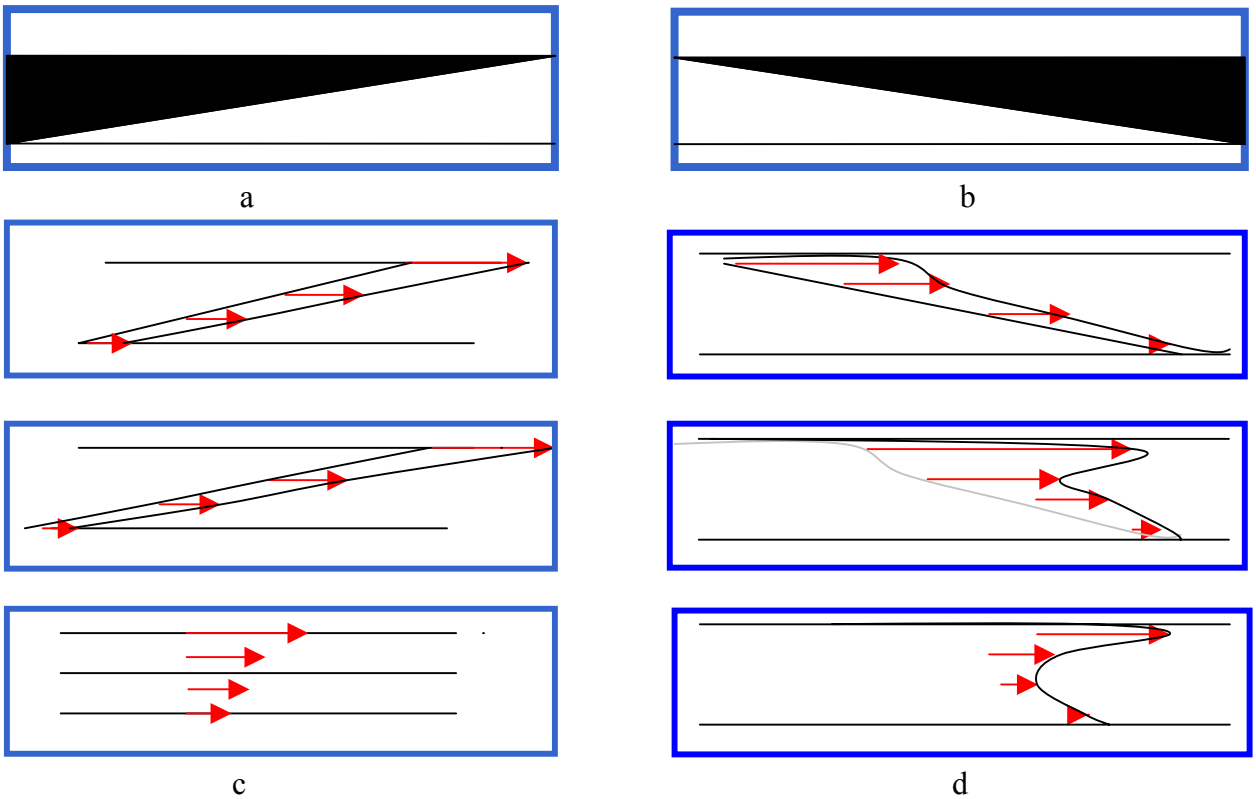

Fig. 5 Cartoons illustrating how the interface between large (black) and small (white) beads is advected by the velocity field when the slope of the interface is positive (5a) and negative (5b). A positive slope corresponds to an increasing percentage of large beads in time, whereas a negative slope corresponds to a decreasing percentage of large beads in time. The interface with a positive slope is advected down to a horizontal position (5c), while the interface with a negative slope undergoes *wave breaking* (5d), as described in the text.

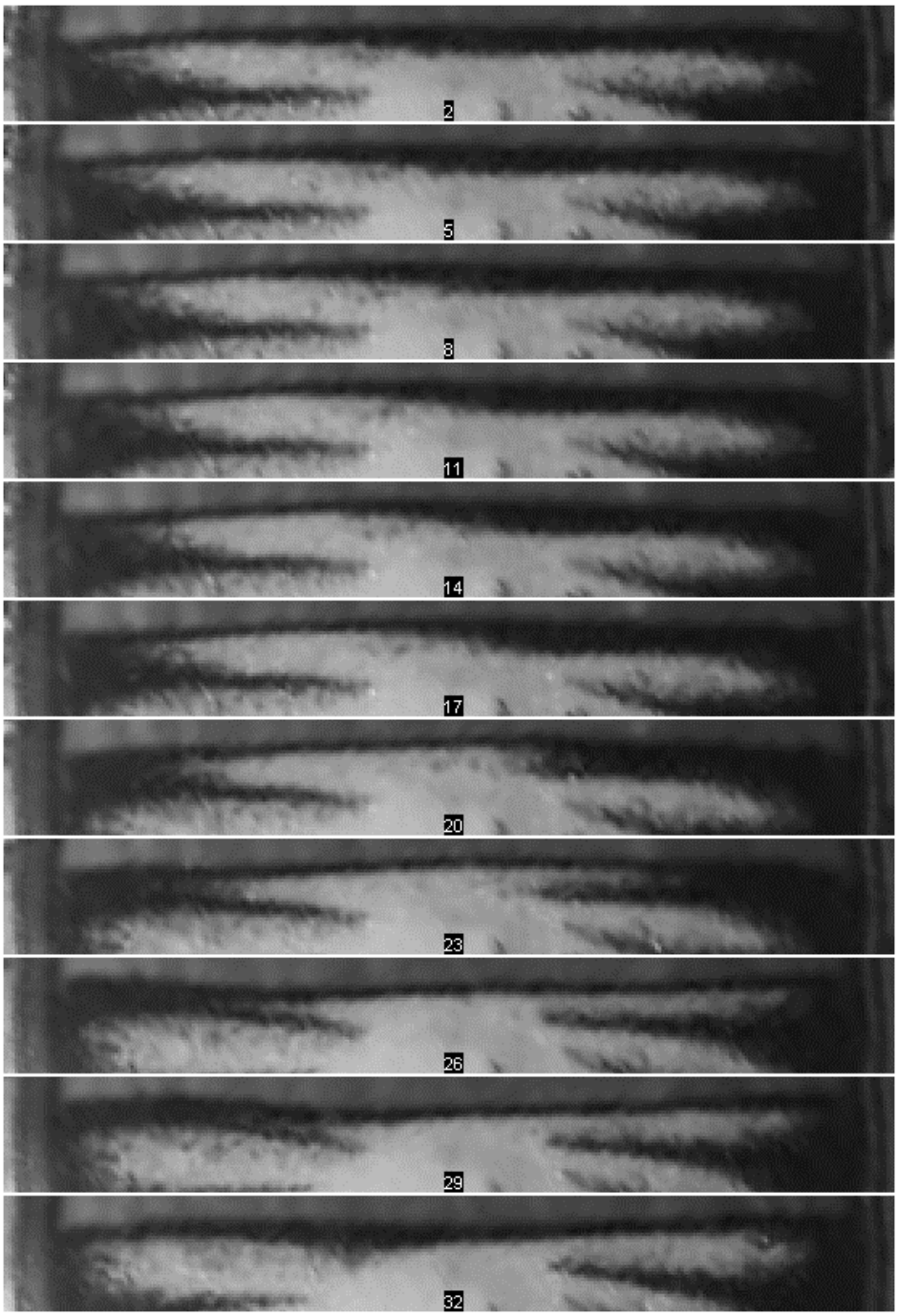

Fig. 6 A series of photographs of showing the wave breaking of an interface between large and small beads. The numbers refer to frames in a video taken at 30 frames per second. The free surface is visible at the top of each photograph. The upper half of the photograph corresponds approximately to the flowing layer. The dark beads are large (dia ~2mm) and the white beads are small (dia ~0.8mm)

Now we consider how the thickness of the stripes varies with the angular velocity of the drum. The preceding discussion indicates that the stripes originate in wave-breaking events within the flowing layer and, therefore, that the thickness of the stripes is bound by the thickness of the flowing layer. Since the thickness of the flowing layer increases with the angular velocity of the drum [4, 6], it follows that the thickness of the stripes should increase (and therefore the number of stripes decrease) as a result of an increase in the angular velocity. This trend is indeed confirmed by the experimental results shown in the first column of Fig. 7. The photographs in this column show the steady patterns for five angular velocities at a single fill level of about 50%. The same trend is observed at other fill levels close to 50% as shown in the second and third columns of Fig. 7.

5. CONCLUSIONS

We have studied experimentally the evolution of striped patterns starting from semi-circular segregation patterns in rotating granular mixtures. The stripes appear to form by amplification of the marginal waviness of semi-circular radial segregation patterns over a time span of tens of rotations. Further, if the angular velocity of the drum increases then the thickness of the stripes increases as well. To gain some insight into the evolution and the characteristics of the striped segregation patterns, we have focused on the flowing layer in whose narrow domain all relative motion between beads is confined. The flowing layer is segregated parallel to the free surface, with the large beads in the upper part and the small beads in the lower part. By studying how the interface between the small and large beads is advected by the velocity field in the flowing layer, we concluded that the formation of stripes may be ascribed to a wave-breaking phenomenon whereby the upper portion of the interface overtakes the lower portion to rush forward and freeze as a stripe upon leaving the boundary layer. We have documented experimentally one of these wave-breaking events in a series of photographs. This series of photographs indicates that the thickness of the stripes is bounded above by the thickness of the flowing layer. This fact, together with the fact that a higher angular velocity leads to an increase in the thickness of the flowing layer, explains the correlation observed in our experiments between the angular velocity and the thickness of the stripes.

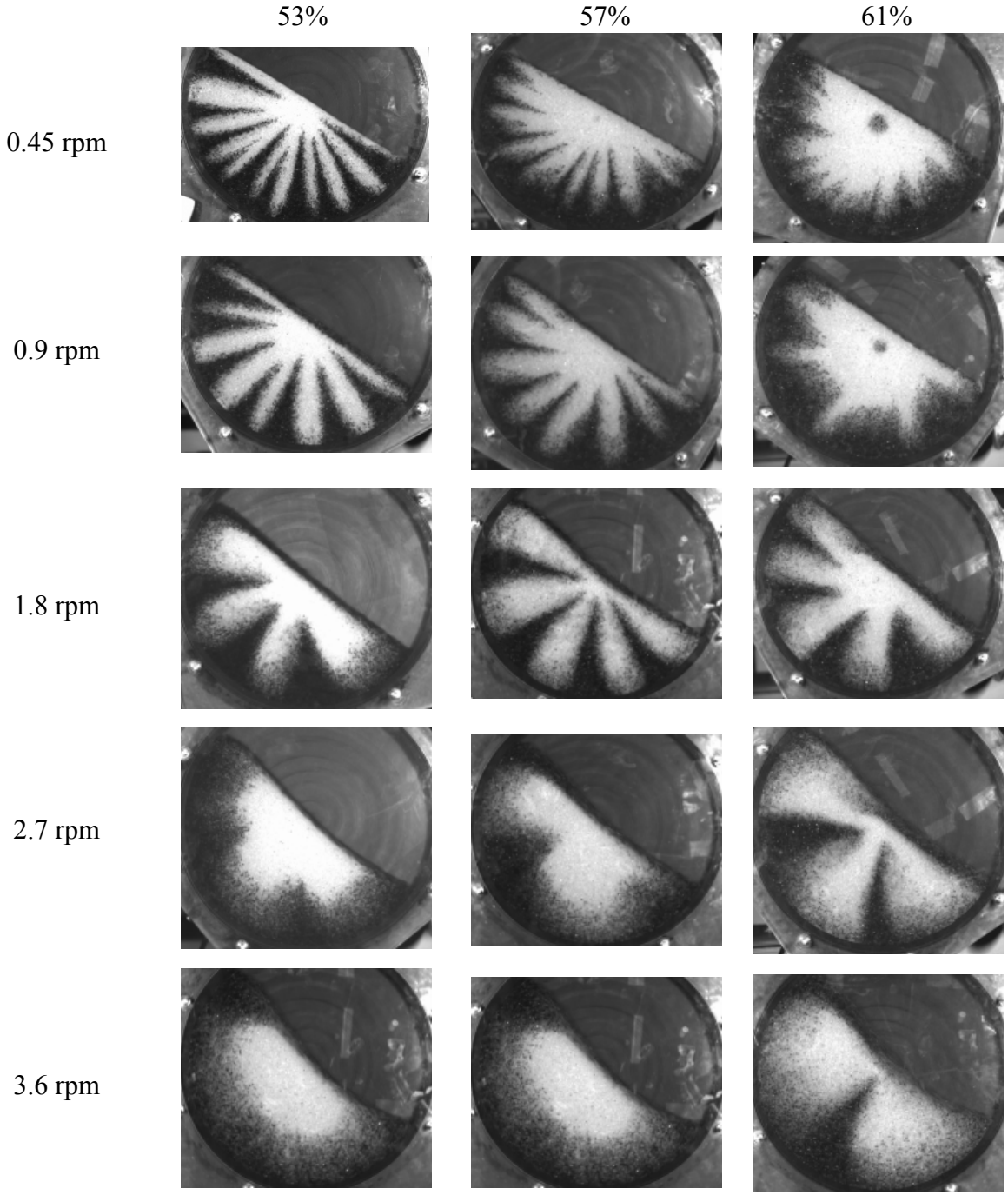

Figure 7. The pictures in this chart show the steady striped segregation pattern as they vary with angular velocities. The first column in this chart shows how the steady striped radial segregation patterns vary with angular velocity for a fill level of about 50%. Experiments at different fill levels, the second and third columns (60% and 70%, respectively), show that the same trend occurs regardless of fill level.

ACKNOWLEDGMENTS

We would like to gratefully acknowledge the support of the UIUC Research board and the UIUC Critical Research Initiation Program for their support.

REFERENCES

1. F. Cantelaub and D. Bideau, 1995, Radial segregation in a 2d drum: An experimental analysis, *Europhysics Letters* **30**: 133–138.
2. E. Clement, J. Rajchenbach, and J. Duran, 1995, Mixing of a granular material in a bidimensional rotating drum *Europhysics Letters* **30**: 7–12.
3. K.M. Hill, J.F. Gilchrist, D.V. Khakhar, J.J. McCarthy, and J.M. Ottino, 1999, Segregation-driven organization in chaotic granular flows. PNAS 96: 11701–11706.
4. S.E. Ott-Monsivais, K.M. Hill, and G. Gioia, 2003, Experimental investigation of dense free surface granular flow, *Proceedings of the 5th Annual Undergraduate Research Conference in Mechanics*: 12–23 (in this volume).
5. K. M. Hill, G. Gioia, and D. Amaravadi, 2003. Striped segregation patterns in a rotating drum: Waviness selection, *submitted*.
6. K.M. Hill, G. Gioia, and V.V. Tota, 2003, Structure and kinematics in dense free-surface granular flow, *Physical Review Letters* **91**, 064302.

List of Recent TAM Reports

No.	*Authors*	*Title*	*Date*
957	Chaïeb, S., and J. Sutin	Growth of myelin figures made of water soluble surfactant—Proceedings of the 1st Annual International IEEE–EMBS Conference on Microtechnologies in Medicine and Biology (October 2000, Lyon, France), 345–348	Oct. 2000
958	Christensen, K. T., and R. J. Adrian	Statistical evidence of hairpin vortex packets in wall turbulence—*Journal of Fluid Mechanics* **431**, 433–443 (2001)	Oct. 2000
959	Kuznetsov, I. R., and D. S. Stewart	Modeling the thermal expansion boundary layer during the combustion of energetic materials—*Combustion and Flame*, in press (2001)	Oct. 2000
960	Zhang, S., K. J. Hsia, and A. J. Pearlstein	Potential flow model of cavitation-induced interfacial fracture in a confined ductile layer—*Journal of the Mechanics and Physics of Solids*, **50**, 549–569 (2002)	Nov. 2000
961	Sharp, K. V., R. J. Adrian, J. G. Santiago, and J. I. Molho	Liquid flows in microchannels—Chapter 6 of *CRC Handbook of MEMS* (M. Gad-el-Hak, ed.) (2001)	Nov. 2000
962	Harris, J. G.	Rayleigh wave propagation in curved waveguides—*Wave Motion* **36**, 425–441 (2002)	Jan. 2001
963	Dong, F., A. T. Hsui, and D. N. Riahi	A stability analysis and some numerical computations for thermal convection with a variable buoyancy factor—*Journal of Theoretical and Applied Mechanics* **2**, 19–46 (2002)	Jan. 2001
964	Phillips, W. R. C.	Langmuir circulations beneath growing or decaying surface waves—*Journal of Fluid Mechanics* (submitted)	Jan. 2001
965	Bdzil, J. B., D. S. Stewart, and T. L. Jackson	Program burn algorithms based on detonation shock dynamics—*Journal of Computational Physics* (submitted)	Jan. 2001
966	Bagchi, P., and S. Balachandar	Linearly varying ambient flow past a sphere at finite Reynolds number: Part 2—Equation of motion—*Journal of Fluid Mechanics* **481**, 105–148 (2003) (with change in title)	Feb. 2001
967	Cermelli, P., and E. Fried	The evolution equation for a disclination in a nematic fluid—*Proceedings of the Royal Society A* **458**, 1–20 (2002)	Apr. 2001
968	Riahi, D. N.	Effects of rotation on convection in a porous layer during alloy solidification—Chapter 12 in *Transport Phenomena in Porous Media* (D. B. Ingham and I. Pop, eds.), 316–340 (2002)	Apr. 2001
969	Damljanovic, V., and R. L. Weaver	Elastic waves in cylindrical waveguides of arbitrary cross section—*Journal of Sound and Vibration* (submitted)	May 2001
970	Gioia, G., and A. M. Cuitiño	Two-phase densification of cohesive granular aggregates—*Physical Review Letters* **88**, 204302 (2002) (in extended form and with added co-authors S. Zheng and T. Uribe)	May 2001
971	Subramanian, S. J., and P. Sofronis	Calculation of a constitutive potential for isostatic powder compaction—*International Journal of Mechanical Sciences* (submitted)	June 2001
972	Sofronis, P., and I. M. Robertson	Atomistic scale experimental observations and micromechanical/continuum models for the effect of hydrogen on the mechanical behavior of metals—*Philosophical Magazine* (submitted)	June 2001
973	Pushkin, D. O., and H. Aref	Self-similarity theory of stationary coagulation—*Physics of Fluids* **14**, 694–703 (2002)	July 2001
974	Lian, L., and N. R. Sottos	Stress effects in ferroelectric thin films—*Journal of the Mechanics and Physics of Solids* (submitted)	Aug. 2001
975	Fried, E., and R. E. Todres	Prediction of disclinations in nematic elastomers—*Proceedings of the National Academy of Sciences* **98**, 14773–14777 (2001)	Aug. 2001
976	Fried, E., and V. A. Korchagin	Striping of nematic elastomers—*International Journal of Solids and Structures* **39**, 3451–3467 (2002)	Aug. 2001
977	Riahi, D. N.	On nonlinear convection in mushy layers: Part I. Oscillatory modes of convection—*Journal of Fluid Mechanics* **467**, 331–359 (2002)	Sept. 2001

List of Recent TAM Reports (cont'd)

No.	*Authors*	*Title*	*Date*
978	Sofronis, P., I. M. Robertson, Y. Liang, D. F. Teter, and N. Aravas	Recent advances in the study of hydrogen embrittlement at the University of Illinois—Invited paper, Hydrogen–Corrosion Deformation Interactions (Sept. 16–21, 2001, Jackson Lake Lodge, Wyo.)	Sept. 2001
979	Fried, E., M. E. Gurtin, and K. Hutter	A void-based description of compaction and segregation in flowing granular materials—*Continuum Mechanics and Thermodynamics*, in press (2003)	Sept. 2001
980	Adrian, R. J., S. Balachandar, and Z.-C. Liu	Spanwise growth of vortex structure in wall turbulence—*Korean Society of Mechanical Engineers International Journal* **15**, 1741–1749 (2001)	Sept. 2001
981	Adrian, R. J.	Information and the study of turbulence and complex flow—*Japanese Society of Mechanical Engineers Journal B*, in press (2002)	Oct. 2001
982	Adrian, R. J., and Z.-C. Liu	Observation of vortex packets in direct numerical simulation of fully turbulent channel flow—*Journal of Visualization*, in press (2002)	Oct. 2001
983	Fried, E., and R. E. Todres	Disclinated states in nematic elastomers—*Journal of the Mechanics and Physics of Solids* **50**, 2691–2716 (2002)	Oct. 2001
984	Stewart, D. S.	Towards the miniaturization of explosive technology—Proceedings of the 23rd International Conference on Shock Waves (2001)	Oct. 2001
985	Kasimov, A. R., and Stewart, D. S.	Spinning instability of gaseous detonations—*Journal of Fluid Mechanics* (submitted)	Oct. 2001
986	Brown, E. N., N. R. Sottos, and S. R. White	Fracture testing of a self-healing polymer composite—*Experimental Mechanics* (submitted)	Nov. 2001
987	Phillips, W. R. C.	Langmuir circulations—*Surface Waves* (J. C. R. Hunt and S. Sajjadi, eds.), in press (2002)	Nov. 2001
988	Gioia, G., and F. A. Bombardelli	Scaling and similarity in rough channel flows—*Physical Review Letters* **88**, 014501 (2002)	Nov. 2001
989	Riahi, D. N.	On stationary and oscillatory modes of flow instabilities in a rotating porous layer during alloy solidification—*Journal of Porous Media* **6**, 1–11 (2003)	Nov. 2001
990	Okhuysen, B. S., and D. N. Riahi	Effect of Coriolis force on instabilities of liquid and mushy regions during alloy solidification—*Physics of Fluids* (submitted)	Dec. 2001
991	Christensen, K. T., and R. J. Adrian	Measurement of instantaneous Eulerian acceleration fields by particle-image accelerometry: Method and accuracy—*Experimental Fluids* (submitted)	Dec. 2001
992	Liu, M., and K. J. Hsia	Interfacial cracks between piezoelectric and elastic materials under in-plane electric loading—*Journal of the Mechanics and Physics of Solids* **51**, 921–944 (2003)	Dec. 2001
993	Panat, R. P., S. Zhang, and K. J. Hsia	Bond coat surface rumpling in thermal barrier coatings—*Acta Materialia* **51**, 239–249 (2003)	Jan. 2002
994	Aref, H.	A transformation of the point vortex equations—*Physics of Fluids* **14**, 2395–2401 (2002)	Jan. 2002
995	Saif, M. T. A, S. Zhang, A. Haque, and K. J. Hsia	Effect of native Al_2O_3 on the elastic response of nanoscale aluminum films—*Acta Materialia* **50**, 2779–2786 (2002)	Jan. 2002
996	Fried, E., and M. E. Gurtin	A nonequilibrium theory of epitaxial growth that accounts for surface stress and surface diffusion—*Journal of the Mechanics and Physics of Solids* **51**, 487–517 (2003)	Jan. 2002
997	Aref, H.	The development of chaotic advection—*Physics of Fluids* **14**, 1315–1325 (2002); see also *Virtual Journal of Nanoscale Science and Technology*, 11 March 2002	Jan. 2002
998	Christensen, K. T., and R. J. Adrian	The velocity and acceleration signatures of small-scale vortices in turbulent channel flow—*Journal of Turbulence*, in press (2002)	Jan. 2002
999	Riahi, D. N.	Flow instabilities in a horizontal dendrite layer rotating about an inclined axis—*Journal of Porous Media*, in press (2003)	Feb. 2002

List of Recent TAM Reports (cont'd)

No.	*Authors*	*Title*	*Date*
1000	Kessler, M. R., and S. R. White	Cure kinetics of ring-opening metathesis polymerization of dicyclopentadiene—*Journal of Polymer Science A* **40**, 2373–2383 (2002)	Feb. 2002
1001	Dolbow, J. E., E. Fried, and A. Q. Shen	Point defects in nematic gels: The case for hedgehogs—*Proceedings of the National Academy of Sciences* (submitted)	Feb. 2002
1002	Riahi, D. N.	Nonlinear steady convection in rotating mushy layers—*Journal of Fluid Mechanics* **485**, 279–306 (2003)	Mar. 2002
1003	Carlson, D. E., E. Fried, and S. Sellers	The totality of soft-states in a neo-classical nematic elastomer—*Journal of Elasticity* **69**, 169–180 (2003) with revised title	Mar. 2002
1004	Fried, E., and R. E. Todres	Normal-stress differences and the detection of disclinations in nematic elastomers—*Journal of Polymer Science B: Polymer Physics* **40**, 2098–2106 (2002)	June 2002
1005	Fried, E., and B. C. Roy	Gravity-induced segregation of cohesionless granular mixtures—*Lecture Notes in Mechanics*, in press (2002)	July 2002
1006	Tomkins, C. D., and R. J. Adrian	Spanwise structure and scale growth in turbulent boundary layers—*Journal of Fluid Mechanics* (submitted)	Aug. 2002
1007	Riahi, D. N.	On nonlinear convection in mushy layers: Part 2. Mixed oscillatory and stationary modes of convection—*Journal of Fluid Mechanics* (submitted)	Sept. 2002
1008	Aref, H., P. K. Newton, M. A. Stremler, T. Tokieda, and D. L. Vainchtein	Vortex crystals—*Advances in Applied Mathematics* **39**, in press (2002)	Oct. 2002
1009	Bagchi, P., and S. Balachandar	Effect of turbulence on the drag and lift of a particle—*Physics of Fluids*, in press (2003)	Oct. 2002
1010	Zhang, S., R. Panat, and K. J. Hsia	Influence of surface morphology on the adhesive strength of aluminum/epoxy interfaces—*Journal of Adhesion Science and Technology* **17**, 1685–1711 (2003)	Oct. 2002
1011	Carlson, D. E., E. Fried, and D. A. Tortorelli	On internal constraints in continuum mechanics—*Journal of Elasticity* **70**, 101–109 (2003)	Oct. 2002
1012	Boyland, P. L., M. A. Stremler, and H. Aref	Topological fluid mechanics of point vortex motions—*Physica D* **175**, 69–95 (2002)	Oct. 2002
1013	Bhattacharjee, P., and D. N. Riahi	Computational studies of the effect of rotation on convection during protein crystallization—*Journal of Crystal Growth* (submitted)	Feb. 2003
1014	Brown, E. N., M. R. Kessler, N. R. Sottos, and S. R. White	*In situ* poly(urea-formaldehyde) microencapsulation of dicyclopentadiene—*Journal of Microencapsulation* (submitted)	Feb. 2003
1015	Brown, E. N., S. R. White, and N. R. Sottos	Microcapsule induced toughening in a self-healing polymer composite—*Journal of Materials Science* (submitted)	Feb. 2003
1016	Kuznetsov, I. R., and D. S. Stewart	Burning rate of energetic materials with thermal expansion—*Combustion and Flame* (submitted)	Mar. 2003
1017	Dolbow, J., E. Fried, and H. Ji	Chemically induced swelling of hydrogels—*Journal of the Mechanics and Physics of Solids*, in press (2003)	Mar. 2003
1018	Costello, G. A.	Mechanics of wire rope—Mordica Lecture, Interwire 2003, Wire Association International, Atlanta, Georgia, May 12, 2003	Mar. 2003
1019	Wang, J., N. R. Sottos, and R. L. Weaver	Thin film adhesion measurement by laser induced stress waves—*Journal of the Mechanics and Physics of Solids* (submitted)	Apr. 2003
1020	Bhattacharjee, P., and D. N. Riahi	Effect of rotation on surface tension driven flow during protein crystallization—*Microgravity Science and Technology* **14**, 36–44 (2003)	Apr. 2003
1021	Fried, E.	The configurational and standard force balances are not always statements of a single law—*Proceedings of the Royal Society* (submitted)	Apr. 2003

List of Recent TAM Reports (cont'd)

No.	*Authors*	*Title*	*Date*
1022	Panat, R. P., and K. J. Hsia	Experimental investigation of the bond coat rumpling instability under isothermal and cyclic thermal histories in thermal barrier systems—*Proceedings of the Royal Society of London A*, in press (2003)	May 2003
1023	Fried, E., and M. E. Gurtin	A unified treatment of evolving interfaces accounting for small deformations and atomic transport: grain-boundaries, phase transitions, epitaxy—*Advances in Applied Mechanics*, in press (2003)	May 2003
1024	Dong, F., D. N. Riahi, and A. T. Hsui	On similarity waves in compacting media—*Horizons in Physics*, in press (2003)	May 2003
1025	Liu, M., and K. J. Hsia	Locking of electric field induced non-180° domain switching and phase transition in ferroelectric materials upon cyclic electric fatigue—*Applied Physics Letters*, in press (2003)	May 2003
1026	Liu, M., K. J. Hsia, and M. Sardela Jr.	In situ X-ray diffraction study of electric field induced domain switching and phase transition in PZT-5H—*Journal of the American Ceramics Society* (submitted)	May 2003
1027	Riahi, D. N.	On flow of binary alloys during crystal growth—*Recent Research Development in Crystal Growth*, in press (2003)	May 2003
1028	Riahi, D. N.	On fluid dynamics during crystallization—*Recent Research Development in Fluid Dynamics*, in press (2003)	July 2003
1029	Fried, E., V. Korchagin, and R. E. Todres	Biaxial disclinated states in nematic elastomers—*Journal of Chemical Physics* **119**, 13170–13179 (2003)	July 2003
1030	Sharp, K. V., and R. J. Adrian	Transition from laminar to turbulent flow in liquid filled microtubes—*Physics of Fluids* (submitted)	July 2003
1031	Yoon, H. S., D. F. Hill, S. Balachandar, R. J. Adrian, and M. Y. Ha	Reynolds number scaling of flow in a Rushton turbine stirred tank: Part I—Mean flow, circular jet and tip vortex scaling—*Chemical Engineering Science* (submitted)	Aug. 2003
1032	Raju, R., S. Balachandar, D. F. Hill, and R. J. Adrian	Reynolds number scaling of flow in a Rushton turbine stirred tank: Part II—Eigen-decomposition of fluctuation—*Chemical Engineering Science* (submitted)	Aug. 2003
1033	Hill, K. M., G. Gioia, and V. V. Tota	Structure and kinematics in dense free-surface granular flow—*Physical Review Letters*, in press (2003)	Aug. 2003
1034	Fried, E., and S. Sellers	Free-energy density functions for nematic elastomers—*Journal of the Mechanics and Physics of Solids*, in press (2003)	Sept. 2003
1035	Kasimov, A. R., and D. S. Stewart	On the dynamics of self-sustained one-dimensional detonations: A numerical study in the shock-attached frame—*Physics of Fluids* (submitted)	Nov. 2003
1036	Fried, E., and B. C. Roy	Disclinations in a homogeneously deformed nematic elastomer—*Nature Materials* (submitted)	Nov. 2003
1037	Fried, E., and M. E. Gurtin	The unifying nature of the configurational force balance—*Mechanics of Material Forces* (P. Steinmann and G. A. Maugin, eds.), in press (2003)	Dec. 2003
1038	Panat, R., K. J. Hsia, and J. W. Oldham	Rumpling instability in thermal barrier systems under isothermal conditions in vacuum—*Philosophical Magazine* (submitted)	Dec. 2003
1039	Cermelli, P., E. Fried, and M. E. Gurtin	Sharp-interface nematic–isotropic phase transitions without flow—*Archive for Rational Mechanics and Analysis* (submitted)	Dec. 2003
1040	Yoo, S., and D. S. Stewart	A hybrid level-set method in two and three dimensions for modeling detonation and combustion problems in complex geometries—*Combustion Theory and Modeling* (submitted)	Feb. 2003
1041	Dienberg, C. E., S. E. Ott-Monsivais, J. L. Ranchero, A. A. Rzeszutko, and C. L. Winter	Proceedings of the Fifth Annual Research Conference in Mechanics (April 2002), TAM Department, UIUC (E. N. Brown, ed.)	Feb. 2003